ISSN 0915-633X

NATIONAL INSTITUTE FOR FUSION SCIENCE

HIDENEK: An Implicit Particle Simulation of Kinetic-MHD Phenomena in Three-Dimensional Plasmas

M. Tanaka

(Received – May 7, 1993)

NIFS-224 May 1993

RESEARCH REPORT
NIFS Series

NAGOYA, JAPAN

HIDENEK: An Implicit Particle Simulation of Kinetic-MHD Phenomena in Three-Dimensional Plasmas

Motohiko Tanaka

National Institute for Fusion Science
Furoh-cho, Nagoya 464-01, Japan

Abstract

An advanced "kinetic-MHD" simulation method and its applications to plasma physics are given in this lecture. This method is quite suitable for studying strong nonlinear, kinetic processes associated with large space-scale, low-frequency electromagnetic phenomena of plasmas. A full set of the Maxwell equations, and the Newton-Lorentz equations of motion for particle ions and guiding-center electrons are adopted. In order to retain only the low-frequency waves and instabilities, implicit particle-field equations are derived. The present implicit-particle method is proved to reproduce the MHD eigenmodes such as Alfven, magnetosonic and kinetic Alfven waves in a thermally near-equilibrium plasma. In the second part of the lecture, several physics applications are shown. These include not only the growth of the instabilities of beam ions against the background plasmas and helical kink of the current, but they also demonstrate nonlinear results such as pitch-angle scattering of the ions. Recent progress in the simulation of the Kelvin-Helmholtz instability is also presented with a special emphasis on the mixing of plasma particles.
(Keywords: implicit particle simulation, kinetic-MHD, three dimensions)

Contents

— Lecture at the Spring College on Plasma Physics —
May 24 and 25, 1993. ICTP, Trieste (Italy)

1. Introduction

1.1 Necessity of Kinetic-MHD Simulations

In contrast to a general belief, kinetic processes do play important roles even in MHD-scale phenomena. That is, a nonlinear evolution of low-frequency, kinetic instabilities may be responsible for transport of energy and particles in plasmas. These problems have remained an important but unresolved issue of plasma physics for more than two decades. Meanwhile, as an origin of these instabilities and transport, a certain realm of the high-temperature plasmas has attracted our attention in which the microscopic, kinetic processes strongly affect the macroscopic plasma processes of magnetohydrodynamic (MHD) time-and-space scales.

In fact, many significant phenomena of space and fusion plasmas are known to take place in this kinetic and macroscopic regime. For example, ion kinetic effects on the m=1 kink mode [1] and fusion-produced energetic alpha particles [2] in ignited tokamaks are just a few of important low-frequency, kinetic problems of the magnetically confined fusion studies. In space and astrophysics, we can list more varieties of kinetic and macroscopic plasma phenomena. To name only a few, these are magnetic reconnection whose dissipation layer has a thickness comparable to gyroradius or inertia length of ions [3], and the kinetic Alfven wave which induces substantial wave-particle interactions with its longitudinal (non-MHD) electric field [4].

Since the aforementioned plasma phenomena are frequently accompanied by strong nonlinear processes, a numerical simulation is virtually the only reliable approach in theoretical studies. However, in the past it was difficult to study these nonlinear plasma processes using either the conventional time-explicit / hybrid particle codes or the MHD fluid code. This was precisely attributed to both a kinetic nature of such plasmas and a disparity of their time-and-space scales with currently uninteresting high-frequency, short-wavelength plasma eigenmodes or light waves.

In order to overcome the difficulties to study kinetic-MHD plasma phenomena, several types of epoch-making and advanced simulation methods were devised during the entire 1980's. These methods, which include the electron kinetic effects in clear contrast to the "hybrid particle" code, are well-documented in References [5-8]. As will be reviewed briefly in Section 1.2, the new simulation methods were successfully applied to various nonlinear phenomena in high-temperature plasmas.

To summarize, what has been required to the new type of the kinetic, large (MHD)-scales simulation methods is an ability to treat (1) various kinetic (particle) effects such as the Landau, cyclotron and bounce resonances with low-frequency waves, and those due to finite Larmor radius and complicated particle trajectories, (2) a space-charge electric field and a finite-speed plasma relaxation arising from non-zero electron inertia, and (3) nonlinear plasma processes under the non-microscopic time-and-space scales, *i.e.*, [duration

time] $\gg \omega_{pe}^{-1}, \omega_{ce}^{-1}$ and [spatial scale] $\gg \lambda_e, \rho_e$. Here, ω_{pe}, ω_{ce} are the plasma and cyclotron frequencies, respectively, and λ_e, ρ_e the Debye and gyroradius of the electrons. Moreover, it should be emphasized that magnetically confined plasmas are often strongly magnetized ($\omega_{ce} \geq \omega_{pe}$) and quite inhomogeneous; the strength and orientation of the magnetic field changes in space and time. The electron diamagnetic drift and magnetization currents are important in the finite-beta (temperature) plasmas. In fact, these (equivalent) drift velocities are given by $v_D \sim (cT_e/eB)/\lambda_0 = \frac{1}{2}c\beta_e(\omega_{ce}/\omega_{pe})(c/\lambda_0\omega_{pe})$ where $\beta_e = 8\pi nT_e/B^2$ is the electron beta value and λ_0 is the gradient scale length of density or the ambient magnetic field.

The new particle simulation methods that were developed in early 1980's have realized kinetic simulations of the low-frequency, electromagnetic phenomena including kinetic effects such as orbit effects and Landau damping. In this regard, these new particle methods are qualitatively higher than the so-called "hybrid-particle" method. However, a difficulty with these methods was a small time step $\omega_{ce}\Delta t \leq O(0.1)$ when one wishes to reproduce the diamagnetic and magnetization effects of the electrons in high magnetic field, high-beta plasmas. By contrast, the uniqueness of the present simulation method is its ability to treat these diamagnetic drift and magnetization effects under a much larger time step $\omega_{ce}\Delta t \gg 1$. This permits us more efficient and accurate simulations of strongly magnetized, high-beta plasmas with much less time steps. (It is also possible for the present method to choose the full-kinetic electrons where the ambient magnetic field is weak or absent (cf. Section 2.1)). In the following paragraphs, several large time-and-space scale, kinetic simulation methods are briefly reviewed.

1.2 Various Methods for Kinetic-MHD Simulations

The first successful implicit simulation method might be the moment implicit method which derives the implicit moment equations to obtain the future electromagnetic field [9-11]. The moment equations involve a divergence of the pressure tensor which, by relying on the fluid concept, is related to the particle velocity moments to achieve a closure of the moment equations. The velocity moments are calculated once in each time step by summations over the particles. This class of the particle code known as the "VENUS" code was developed at Los Alamos National Laboratory in early 1980's and was applied to laser irradiation and various beam-plasma processes [12]. However, the assumptions used in relating the pressure tensor with the particle moments restricted the time step to a moderate value $\omega_{pe}\Delta t \leq 10$ in warm kinetic plasma simulations. An improved method recently outgrew from the moment implicit method to treat the warm plasmas with a large time step, and several demonstrations were made for one-dimensional plasmas (CELEST) [13].

The closely-coupled implicit method, which this lecture is going to present, was devised in early 1984 as an electromagnetic simulation method for multi-dimensional plasmas by

following the intuition that the futureward time-shifted electromagnetic field might act to preferentially suppress high frequency oscillations in the plasma [7]. Now this method satisfies the aforementioned three points and additional one that are required to the large-scales kinetic simulation methods [14]. The technically most characteristic feature of this implicit method, which is implemented in the HIDENEK code[1] is a direct determination of the future electromagnetic field using completely implicit, coupled kinetic equations. Here, a predictor-corrector particle push is not used to obtain unknown current and charge densities which act as driving forces in the field equations. Hence, these coupled kinetic equations are named "closely-coupled field-particle (CCFP) equations."

Another type of the implicit electromagnetic particle simulation method which is called the direct implicit method was developed at Livermore National Laboratory and the University of Texas [15,16]. This method constructs a high-accuracy low-pass time filter by combining the electric acceleration of a few time levels in the equations of motion to control numerical damping of high-frequency waves in the plasma. The future current density is explicitly predicted by pushing particles and is implicitly corrected later in the field equations. A recent progress in the filtering technique is found in Reference [17]. Basically, the direct implicit method has the second-order (or more) accuracy in time, however, it suffered from substantial and monotonic loss of the particle kinetic energy during the course of the two-dimensional simulation [16].

The gyrokinetic particle simulation method [8] which was motivated at the Princeton Plasma Physics Laboratory is conceptually different from the implicit particle methods in that it derives reduced field equations by gyro-averaging the ion response under assumptions of smallness on the wavelength and frequency $k_{\parallel}/k_{\perp} \ll 1$, $\omega/\omega_{ci} \ll 1$ and those on the amplitude of the electromagnetic field. Many insignificant terms are removed from the original kinetic equations. Efficiency and accuracy of the simulation are therefore quite reasonable when the ordering assumptions are satisfied. However, when the assumptions become marginally satisfied which occurs with large electrostatic disturbances $e\delta\varphi/T_e \sim O(1)$ at the plasma edge, for example, or magnetic perturbations $\delta B/B_0 \sim O(1)$ at the magnetic reconnection, many correction terms are required to make the simulation physically meaningful.

As possibly a comparable kinetic simulation method with the implicit particle methods, the hybrid particle code with particle ions and massless electrons is sometimes used for the study of low-frequency electromagnetic phenomena [18]. The hybrid code is quite efficient since the electron kinetic effects are excluded; it is considered to be valid when the electron inertia effects are completely ignorable. This is the case with a simulation of the perpendicular magnetosonic shock where the plasma is strongly magnetized with the magnetic field lying perpendicularly to the simulation plane [19]. However, the hybrid code becomes increasingly unjustifiable as the magnetic field becomes more oblique or parallel to

[1]HIDENEK was named after a Japanese god. Also, a word "HIDEN" means magic and secret skills.

the simulation plane so that the electrons are allowed to move along the ambient magnetic field through an inhomogeneous medium.

1.3 Characteristics of the Closely-Coupled Implicit Method

The essense of the closely-coupled implicit method is qualitatively described in some depth. There was a preliminary ("semi-implicit") version which was first developed and applied to variety of large space-scale simulations such as an excitation of the kinetic Alfven wave and associated plasma heating [20], and current-beam injection and kink instability [21]. However, the time step was limited to $\omega_{pe}\Delta t \leq 1$. Qualitatively much improved version that can deal with "homogeneous" kinetic plasmas in large time-and-space scales was then developed [7]. The characteristics of the algorithm were extensively studied and its validity was proved both analytically and numerically in the literature. Recently the latter version of the code has greatly been upgraded so that it can efficiently deal with high magnetic field, high-beta kinetic plasmas in large(MHD)-scales [14]. Specifically, the guiding-center approximation with the magnetic effects has been introduced to the electron motion. The parallel motion along the magnetic field line is traced as particles in a drift-kinetic fashion with $-\mu\nabla_{\parallel}B$ force included. This enables us the treatment of the diamagnetic and magnetization currents while eliminating both the high-frequency electron cyclotron and plasma oscillations. These time scales are of the same orders of magnitude in the magnetically confined plasmas.

- Large time-and-space scales: $\omega_{pe}\Delta t \gg 1$, $\omega_{ce}\Delta t \gg 1$, and $\Delta x \geq c/\omega_{pe}$.
- Electromagnetic.
- Multi-dimensions in any geometry (Cartesian, cylinder, torus).
- Inhomogeneous plasma density and magnetic field.
- Kinetic:
  - Ions: Full particle dynamics in 3-D.
  - Electrons: Parallel direction $\rightarrow$ 1-D motion with $(-\mu\nabla_{\parallel}B)$ force.
    Perpendicular direction $\rightarrow$ Guiding-center drift motion.
    ($\mathbf{E}\times\mathbf{B}$, ∇B, curvature drifts)

$\rightarrow$
- Resonance effects (Landau, cyclotron, bounce resonances)
- Orbit effects: Finite Larmor radius effects
  Diamagnetic and magnetization effects
  Complicated particle orbits
- Finite speed relaxation due to electron inertia

} included.

Table 1. Characteristics of the HIDENEK Simulation.

In a word, the key of the closely-coupled implicit method consists in the complete time-implicitness. By combining the Maxwell equations with the equations of motion of particles, the closely-coupled field-particle equations are derived which directly determine the future electromagnetic field without an auxiliary prediction of the current and charge densities. These equations are solved in the real (configuration) space because the implicitly-expressed current and charge densities, which are the major driving terms of the equations, vary considerably in space for inhomogeneous plasmas. This makes the solution in the Fourier-space difficult and inefficient. The characteristic features of the closely-coupled implicit method are summarized in Table 1. The fundamentally important feature here is that the low-frequency electromagnetic waves and structures with $\omega_0 \Delta t \ll 1$ are properly reproduced, where ω_0 is their characteristic frequency and Δt the time step of the simulation. Since the ions and electrons are handled as the particle species, various particle orbit effects are well simulated by this method. Moreover, the method works numerically well both in the linear and nonlinear stages of the plasma processes by virtue of the slightly backward time-decentered scheme. These advanced features make the closely-coupled implicit method quite suitable for studies of the nonlinear, kinetic plasma phenomena occurring in large time-and-space scales.

2. Algorithm for Low-Frequency Kinetic Plasma Simulation

This section gives the fundamental equations governing the electromagnetic field and particle motion in the closely-coupled implicit method. These equations are discretized in time using the finite-difference scheme. Then, the Courant-condition-free, implicit equations are derived which determine the future electromagnetic field in a large time step compared to the electron time scales. Finally, the necessity of an implicit correction to the longitudinal (curl-free) part of the electric field is discussed.

2.1 Fundamental Equations of Field and Particles

In order to realize a kinetic simulation of plasmas in large time-and-space scales, we introduce a slightly backward time-decentered scheme. The Maxwell equations are used to describe the electromagnetic field which with time level suffices are written

$$\frac{1}{c}\left(\frac{\partial \mathbf{E}}{\partial t}\right)^{n+1/2} = \nabla \times \mathbf{B}^{n+\alpha} - \frac{4\pi}{c}\,\mathbf{j}^{n+\alpha}, \tag{1}$$

$$\frac{1}{c}\left(\frac{\partial \mathbf{B}}{\partial t}\right)^{n+1/2} = -\nabla \times \mathbf{E}^{n+\alpha}, \tag{2}$$

$$\nabla \cdot \mathbf{E}^{n+1} = 4\pi\rho^{n+1}, \tag{3}$$

$$\nabla \cdot \mathbf{B}^{n+1} = 0. \tag{4}$$

Here, $\mathbf{E}$ and $\mathbf{B}$ are the electric and magnetic fields, respectively, c is the speed of light, and α is a decentering (implicitness) parameter to be specified later. The current density $\mathbf{j}$ and

the charge density ρ are implicit quantities which are to be expressed as the functions of unknown electromagnetic fields in Section 2.3.

The equations of motion for the ions are the standard Newton-Lorentz equations except the time level of the electromagnetic field which are given by

$$\left(\frac{d\mathbf{v}_j}{dt}\right)^{n+1/2} = \frac{e_i}{m_i}\left[\mathbf{E}^{n+\alpha}(\mathbf{x}_j) + (\mathbf{v}_j^{n+1/2}/c) \times \mathbf{B}^{n+\alpha}(\mathbf{x}_j)\right], \tag{5}$$

$$\left(\frac{d\mathbf{x}_j}{dt}\right)^{n+1/2} = \mathbf{v}_j^{n+1/2}. \tag{6}$$

The choice of the same time level $t = t^{n+\alpha}$ for the electric and magnetic fields, which is required to properly reproduce the Ponderomotive force of the electromagnetic and Alfven waves (See Section 7.3 of [14]), differs from other implicit algorithms [11-13,15,16]. By contrast, the velocity in the Lorentz term must be exactly time-centered to preserve the cyclotron motion.

For the motion of the electrons, there are two options. The first one is to use the Newton-Lorentz equations, Eqs.(5) and (6), as for the ions, which allows us a fully-kinetic simulation of the plasma. However, to retain the cyclotron orbit effects such as diamagnetic drift and magnetization currents, a rather small time step $\omega_{ce}\Delta t \sim O(0.1)$ is required. On the contrary, we choose the second option of introducing the guiding-center approximation in order to eliminate the electron cyclotron time-scale ω_{ce}^{-1}. The equations of motion are decomposed into the parallel and perpendicular components with respect to the local magnetic field, which are given by

$$\left(\frac{dv_{\|j}}{dt}\right)^{n+1/2} = \left(\frac{-e}{m_e}\right)E_{\|}^{n+\alpha} - \left(\frac{\mu_j}{m_e}\right)\frac{\partial}{\partial x_{\|}}B^{n+\alpha} \tag{7}$$

$$\mathbf{v}_{\perp j}^{n+\alpha} = c\left(\frac{\mathbf{E}\times\mathbf{B}}{B^2}\right)^{n+\alpha} + \left\{\left(\frac{m_e c}{-eB}\right)\mathbf{b}\times\left(\frac{\mu_j}{m_e}\nabla B + v_{\|j}^2\frac{\partial \mathbf{b}}{\partial x_{\|}}\right)\right\}^{n+\alpha}, \tag{8}$$

$$\left(\frac{d\mathbf{x}_j}{dt}\right)^{n+1/2} = (\mathbf{v}_{\|j}^{n+1/2} + \mathbf{v}_{\perp j}^{n+\alpha}). \tag{9}$$

In Eq.(7), $v_{\|j}$ is a scalar velocity (sign included) along the magnetic field and $\mu_j = \left(\frac{1}{2}m_e v_{th,j}^2/B(\mathbf{x}_j)\right)_{t=0}$ $(= const.)$ is the magnetic moment of the j-th electron with $v_{th,j}$ being its thermal velocity. The unit vector along the magnetic field line $\mathbf{b} = (\mathbf{B}/B)$ is defined locally at each particle position. The three terms of Eq.(8) represent the $E \times B$, gradient-B and curvature drifts, respectively.

It is important to note that the time indices of each term in Eqs.(7)–(9) must be consistent with their counterparts in the Newton-Lorentz equation. For example, the time level of the perpendicular velocity in Eq.(9) should be $t = t^{n+\alpha}$. Otherwise, the electrons

and ions would show different responses ($E \times B$ drift, etc.) to the low-frequency component of the electromagnetic field. The vector "parallel" velocity in Eq.(9) is defined by

$$\mathbf{v}_{\|j}^{n+1/2} = v_{\|j}^{n+1/2}\, \mathbf{b}^{n+\alpha}(\mathbf{x}_j). \tag{10}$$

The parallel electric field and the differential operator are defined, respectively, by $E_{\|}^{n+\alpha} = (\mathbf{b}^{n+\alpha} \cdot \mathbf{E}^{n+\alpha})$ and $\partial/\partial x_{\|} = (\mathbf{b}^{n+\alpha} \cdot \nabla)$. (Refer to the paragraph in Section 2.2 containing Eq.(13) for the proof.)

The parameter α appearing in the Maxwell equations and the equations of motion controls the degree of numerical damping of high-frequency oscillations. The parameter α must be always larger than $\frac{1}{2}$ and in the range $\frac{1}{2} < \alpha \leq 1$. As is shown in [14], the decentering of the time level in the curl terms of Eqs.(1),(2) causes damping of high-frequency light waves. Attenuation of high-frequency electromagnetic and electrostatic waves with $\omega\Delta t \geq O(1)$ which arise from the plasma responses is accomplished by the decentering of the electric and magnetic fields in the equations of motion [7]. Since a large time step $\omega_{pe}\Delta t \gg 1$ is generally used, the Langmuir oscillations are eliminated. A discussion is found in Reference [14] about how the numerical stability and energy conservation of the simulation are affected by the choice of the parameter α.

2.2 The Field and Particle Equations in the Finite Difference Form

The field and particle equations given in Section 2.1 are time-discretized using the finite difference scheme. The first equation of motion for the ions is written

$$\mathbf{v}_j^{n+1} = \mathbf{v}_j^n + \Delta t \frac{e_i}{m_i} [\tilde{\mathbf{E}}^{n+\alpha} + (\mathbf{v}_j^{n+1/2}/c) \times \tilde{\mathbf{B}}^{n+\alpha}], \tag{11}$$

where Δt is a time step and the velocity is defined on the integer time level as well as the position of the particles to be mentioned later. The tilde quantity stands for the field that is evaluated at the predicted particle position $\bar{\mathbf{x}}_j$ using the linear interpolation (area-weighting) of the field value which is defined on the neighborhood grids $\mathbf{x}_g$,

$$\tilde{\mathbf{E}}(\bar{\mathbf{x}}_j) \equiv \sum_g \mathbf{E}(\mathbf{x}_g) S(\mathbf{x}_g - \bar{\mathbf{x}}_j). \tag{12}$$

Here, $S(\mathbf{x})$ is the weight function satisfying $\int S(\mathbf{x}) d\mathbf{x} = 1$ which acts to connect the particle (Lagrange) and field (Eulerian) quantities. The "predicted" position to evaluate the electric and magnetic fields is the mid-point of orbits which is defined by $\bar{\mathbf{x}}_j^{n+1/2} = \mathbf{x}_j^n + \frac{1}{2}\Delta t\, \mathbf{v}_{j(0)}^{n+1/2}$ where $\mathbf{v}_{j(0)}^{n+1/2}$ is the velocity calculated by means of only the known field values at $t = t^n$. The choice of the mid-point is particularly important for the magnetic field in the Lorentz term of Eq.(11) to avoid fictious drifts of particles. For the trapped particles, a special care might be required to predict their future positions accurately around the turning points.

We solve Eq.(11) in terms of $\mathbf{v}_j^{n+1}$ using the interpolation $\mathbf{v}^{n+1/2} = \frac{1}{2}(\mathbf{v}^n + \mathbf{v}^{n+1})$ to obtain

$$\mathbf{v}_j^{n+1} = \mathbf{v}_j^n + \Delta t \frac{e_i}{m_i} \{ \left(\tilde{\mathbf{E}}^{n+\alpha} + \frac{\mathbf{v}_j^n}{c} \times \tilde{\mathbf{B}}^{n+\alpha} \right) + \Theta^2 \tilde{\mathbf{E}}_{\|}^{n+\alpha}$$

$$+ \Theta \left(\tilde{\mathbf{E}}^{n+\alpha} + \frac{\mathbf{v}_j^n}{c} \times \tilde{\mathbf{B}}^{n+\alpha} \right) \times \tilde{\mathbf{b}}^{n+\alpha} \} / (1+\Theta^2), \tag{13}$$

$$\mathbf{x}_j^{n+1} = \mathbf{x}_j^n + \Delta t \, \mathbf{v}_j^{n+1/2}, \tag{14}$$

where $\tilde{\mathbf{E}}_{\parallel}^{n+\alpha} = (\tilde{\mathbf{E}}^{n+\alpha} \cdot \tilde{\mathbf{b}}^{n+\alpha}) \, \tilde{\mathbf{b}}^{n+\alpha}$, $\Theta(\mathbf{x}) = \frac{1}{2}\Delta t (e_i/m_i c) |\tilde{\mathbf{B}}|^{n+\alpha}$. It is mentioned in passing that the first term in the right-hand side of Eq.(13), $\mathbf{v}_j^n$, has been intentionally separated out of the denominator $(1+\Theta^2)$ which includes the future magnetic field $\mathbf{B}^{n+\alpha}$. In the $|\Theta| \gg 1$ limit which corresponds to the guiding-center approximation, the first-order terms yield

$$\mathbf{v}_j^{n+1} \cong \mathbf{v}_j^n + \Delta t \frac{e_j}{m_j} \{ \tilde{\mathbf{E}}_{\parallel}^{n+\alpha} + \frac{1}{\Theta} \left(\tilde{\mathbf{E}}^{n+\alpha} + \frac{\mathbf{v}_j^n}{c} \times \tilde{\mathbf{B}}^{n+\alpha} \right) \times \tilde{\mathbf{b}}^{n+\alpha} \}. \tag{15}$$

Decomposition of the parallel and perpendicular components in terms of the direction of the magnetic field $\mathbf{b}^{n+\alpha}$ gives

$$\mathbf{v}_{\perp j}^{n+1} \cong c\tilde{\mathbf{E}}^{n+\alpha} \times \tilde{\mathbf{b}}^{n+\alpha} / B^{n+\alpha} \tag{16}$$

$$v_{\parallel j}^{n+1} \cong v_{\parallel j}^n + \Delta t \frac{e_j}{m_j} (\tilde{\mathbf{E}}^{n+\alpha} \cdot \tilde{\mathbf{b}}^{n+\alpha}). \tag{17}$$

These are the leading terms of the guiding-center equations of motion Eqs.(7)–(8).

The equations of motion for the electrons Eqs.(7)-(9) are similarly discretized in time and are given by

$$v_{\parallel j}^{n+1} = v_{\parallel j}^n + \Delta t \left(\left(\frac{-e}{m_e} \right) \tilde{E}_{\parallel}^{n+\alpha} - \left(\frac{\mu_j}{m_e} \right) \frac{\partial}{\partial x_{\parallel}} \tilde{B}^{n+\alpha} \right), \tag{18}$$

$$\mathbf{x}_j^{n+1} = \mathbf{x}_j^n + \Delta t \, \{ \mathbf{v}_{\parallel j}^{n+1/2} + \mathbf{v}_{\perp j}^{n+\alpha}(\bar{\mathbf{x}}_j^{n+1/2}) \}. \tag{19}$$

The perpendicular velocity is a function of the future electromagnetic field as specified by Eq.(8), and the direction of the parallel velocity is defined with respect to $\mathbf{b}^{n+\alpha}$ by Eq.(10).

The Maxwell equations are discretized with respect to time and are written

$$\mathbf{E}^{n+1} - \mathbf{E}^n = c\Delta t \nabla \times \mathbf{B}^{n+\alpha} - 4\pi \Delta t \, \mathbf{j}^{n+\alpha}, \tag{20}$$

$$\mathbf{B}^{n+1} - \mathbf{B}^n = -c\Delta t \nabla \times \mathbf{E}^{n+\alpha}. \tag{21}$$

In order to avoid the Courant condition which severely restricts magnitude of the time step against the given space grid intervals, we eliminate $\mathbf{B}^{n+1}$ from Eqs.(20)(21) to derive an implicit equation for $\mathbf{E}^{n+1}$. During this algebra, we use for $\mathbf{E}^{n+\alpha}$ the linear interpolation of the field quantity to the non-integer time level

$$\mathbf{E}^{n+\alpha} = \alpha \mathbf{E}^{n+1} + (1-\alpha)\mathbf{E}^n, \tag{22}$$

and a similar interpolation for $\mathbf{B}^{n+\alpha}$. This procedure yields the equation to determine the future electric field $\mathbf{E}^{n+1}$,

$$\begin{aligned} [\, 1 + (\alpha c \Delta t)^2 \nabla \times \nabla \times \,] \, \mathbf{E}^{n+1} = {} & [\, 1 - \alpha(1-\alpha)(c\Delta t)^2 \nabla \times \nabla \times] \, \mathbf{E}^n \\ & + c\Delta t \nabla \times \mathbf{B}^n - 4\pi \Delta t \, \mathbf{j}^{n+\alpha}. \end{aligned} \tag{23}$$

Here, the $\nabla \times \mathbf{B}^{n+\alpha}$ term has been split to the $\nabla \times \mathbf{B}^n$ term and the $\nabla \times \nabla \times \mathbf{E}$ terms which appear on the both sides of Eq.(23). The functional form of the current density in the right-hand side of the equation is to be specified in Section 2.3. The future magnetic field is obtained using Eq.(21) once $\mathbf{E}^{n+1}$ has been known.

It is noted that, since the inequality $(c\Delta t/\lambda)^2 \gg 1$ holds ($\nabla\times \approx 1/\lambda$), Eq.(23) is essentially decomposed into the magnetic component $\nabla \times \mathbf{B}^{n+\alpha} = (4\pi/c)\, \mathbf{j}_T^{n+\alpha}$ and the electrostatic component $\mathbf{E}_L^{n+1} = \mathbf{E}_L^n - 4\pi\Delta t\, \mathbf{j}_L^{n+\alpha}$, where (T) and (L) denote the transverse (solenoidal) and longitudinal (curl-free) parts, respectively. The latter equation is equivalently transformed into $(\rho^{n+1} - \rho^n)/\Delta t + \nabla \cdot \mathbf{j}_L^{n+\alpha} = 0$ by using Eq.(3). A deviation of the longitudinal electric field $\mathbf{E}_L^{n+1}$ from the true electric field obtained by $\nabla \cdot \mathbf{E}^{n+1} = 4\pi\rho^{n+1}$ needs to be adjusted later. As has been instructed here, the unity terms in the square brackets make a significant contribution to the electrostatic part and cannot be ignored. Despite of simplicity of the decomposed equations, however, we do not use them in the simulation. The reason against them is that the above magnetoinductive (Darwin) algorithm requires a complete separation of the transverse current $\mathbf{j}_T$ ($\nabla \cdot \mathbf{j}_T = 0$) from the longitudinal current $\mathbf{j}_L$ ($\nabla \times \mathbf{j}_L = 0$). This is a non-trivial operation in the real-space and for the implicit current density given in the next subsection; an incomplete decomposition of the current components leads to poor accuracy and numerical instability.

2.3 The Closely-Coupled Field-Particle Equations

2.3(a) The Time-Implicit Equations for the Electromagnetic Field

To obtain the future electromagnetic field by Eq.(23), the current density must be specified to have a closure of the equation. A prediction of the current density in the Maxwell equations is the key of the implicit algorithm which must be nonlinearly stable against a large time step. (A prediction without suppression of the high-frequency plasma oscillations may fail for $\omega_{pe}\Delta t \geq 2$.) In the present algorithm, the current density is directly expressed in terms of the future electromagnetic field with the aid of the equations of motion:

$$
\begin{aligned}
\mathbf{j}^{n+\alpha}(\mathbf{x}) &= \sum_j e_j \mathbf{v}_j^{n+\alpha} S(\mathbf{x} - \bar{\mathbf{x}}_j^{n+\alpha}) \\
&= \sum_{j=i} e_i \Big[\mathbf{v}_j^n + \alpha\Delta t \frac{e_i}{m_i} \Big\{ \Big(\tilde{\mathbf{E}}^{n+\alpha} + \frac{\mathbf{v}_j^n}{c} \times \tilde{\mathbf{B}}^{n+\alpha} \Big) + \Theta^2 \tilde{\mathbf{E}}_{\parallel}^{n+\alpha} \\
&\quad + \Theta \Big(\tilde{\mathbf{E}}^{n+\alpha} + \frac{\mathbf{v}_j^n}{c} \times \tilde{\mathbf{B}}^{n+\alpha} \Big) \times \tilde{\mathbf{b}}^{n+\alpha} \Big\} / (1 + \Theta^2) \Big]\, S(\mathbf{x} - \bar{\mathbf{x}}_j^{n+\alpha}) \\
&+ \sum_{j=e} (-e) \Big[\Big\{ v_{\parallel j}^n + \alpha\Delta t \Big(\Big(\frac{-e}{m_e} \Big) \tilde{E}_{\parallel}^{n+\alpha} - \Big(\frac{\mu_j}{m_e} \Big) \frac{\partial}{\partial x_{\parallel}} \tilde{B}^{n+\alpha} \Big) \Big\} \tilde{\mathbf{b}}^{n+\alpha} \\
&\quad + \tilde{\mathbf{v}}_{\perp j}^{n+\alpha}(\bar{\mathbf{x}}_j^{n+1/2}) \Big]\, S(\mathbf{x} - \bar{\mathbf{x}}_j^{n+\alpha}) - c\, \nabla \times \sum_{j=e} \mu_j \tilde{\mathbf{b}}^{n+\alpha} S(\mathbf{x} - \bar{\mathbf{x}}_j^{n+\alpha}), \quad (24)
\end{aligned}
$$

where $\Theta(\mathbf{x}) = \frac{1}{2}\Delta t (e_i/m_i c)|\mathbf{B}|^{n+\alpha}$ and $\mathbf{v}_{\perp j}^{n+\alpha}$ is given by Eq.(8). The last term of Eq.(24) accounts for the magnetization current $\mathbf{j}_M = -c\nabla \times (p_{\perp}^{(e)} \mathbf{b}/B)$ of the electrons under the

guiding-center approximation. The symbols $\sum_{j=i}$ and $\sum_{j=e}$ denote summations over the ion and electron species, respectively. As before, the electromagnetic field with the tilde is evaluated with the weighting scheme Eq.(12). The time level of $\tilde{\mathbf{v}}_{\perp j}$ should be again $t = t^{n+\alpha}$ to be consistent with the ion cross-field response. The basic unknown quantities in the right-hand side of Eq.(24) are $\mathbf{E}^{n+1}$ and $\mathbf{B}^{n+1}$.

Substitution of the implicitly-expressed current density Eq.(24) into Eq.(23) yields the matrix equation to determine the future electric field $\mathbf{E}^{n+1}$,

$$A_v\, \mathbf{E}^{n+1} \;=\; \mathbf{S}_p(\mathbf{E}^n, \mathbf{B}^n;\; \mathbf{E}^{n+1}, \mathbf{B}^{n+1}). \tag{25}$$

The matrix A_v on the left-hand side represents a vacuum response which is defined by

$$A_v \;=\; 1 \;+\; (\alpha c\Delta t)^2(\nabla\nabla - 1\nabla^2), \tag{26}$$

and the source vector $\mathbf{S}_p$ on the right-hand side is given by

$$\begin{aligned}\mathbf{S}_p \;=\; & [1 - \alpha(1-\alpha)(c\Delta t)^2(\nabla\nabla - \nabla^2)]\, \mathbf{E}^n + c\Delta t\, \nabla \times \mathbf{B}^n \\ & - 4\pi\Delta t\, \{\sum_{j=i} e_i\, [\mathbf{v}_j^n + \alpha\Delta t(e_i/m_i) \left(\tilde{\mathbf{E}}^{n+\alpha} + \frac{\mathbf{v}_j^n}{c} \times \tilde{\mathbf{B}}^{n+\alpha}\right) \\ & /(1+\Theta^2)]\, S(\mathbf{x} - \bar{\mathbf{x}}_j^{n+\alpha}) \;+\; \cdots\cdots \}. \end{aligned} \tag{27}$$

The symbol $\nabla\nabla$ denotes a dyadic operator and $\mathbf{1}$ the unit tensor. (Refer to Section 2.4 for further modifications of the above equations.) The equations (25)-(27) and (21) constitute a closed set of the Courant-condition-free, implicit equations to determine the future electromagnetic field. These equations are named "closely-coupled field-particle (CCFP) equations" after their nature of nonlinear coupling of the fields and particles.

2.3(b) A Correction to the Longitudinal Electric Field

The third and fourth Maxwell equations, Eqs.(3) and (4), are the conditions to determine the initial value of the electromagnetic field, and they need not be used mathematically for $t > 0$. However, it must be noted that the time-decentered current density in the Ampere's law, which was used to eliminate high-frequency electromagnetic modes, does not satisfy the continuity of charge density. In fact, a net correction to the electric field is required which is done in the following manner. We put the true electric field $\mathbf{E}^{n+1}$ as a sum of the electric field before the correction $\breve{\mathbf{E}}^{n+1}$ (the solution of Eq.(25)) and the longitudinal (curl-free) correction which is a gradient of the scalar function $\delta\varphi$,

$$\mathbf{E}^{n+1} \;=\; \breve{\mathbf{E}}^{n+1} - \nabla\delta\varphi. \tag{28}$$

Then, after combining the continuity equation and the Ampere's law, a finite-order correction equation for $\delta\varphi$ is given by

$$\nabla^2\delta\varphi \;=\; 4\pi\Delta t\, \nabla\cdot(\mathbf{J}^{n+1/2} - \mathbf{J}^{n+\alpha}). \tag{29}$$

The magnitude of the correction is estimated to be

$$\begin{aligned}\nabla^2\delta\varphi &\cong -4\pi(\alpha-\frac{1}{2})(\Delta t)^2\frac{\partial}{\partial t}\nabla\cdot\mathbf{J}^{n+1/2} \\ &= 4\pi(\alpha-\frac{1}{2})\Delta t\sum_{\mathbf{k}}(i\omega_k\Delta t)\nabla\cdot\mathbf{J}_k^{n+1/2}. \end{aligned} \tag{30}$$

Remember that the right-hand side is a function of $\delta\varphi$. Although $\omega_k\Delta t$ in Eq.(30) is a small quantity for the resolved modes in the implicit simulation, it is inevitable for $\alpha > 1/2$ to make the "divergence correction" to the electric field that has been obtained by solving the coupled field-particle equations of Section 2.2.

Actual correction is made by substituting Eq.(28) into the Gauss's law (3) which includes the charge density ρ^{n+1}. This yields the equation to determine $\delta\varphi$,

$$-\nabla^2\delta\varphi = 4\pi\rho^{n+1} - \nabla\cdot\breve{\mathbf{E}}^{n+1}. \tag{31}$$

Again, the charge density ρ^{n+1} which is not known at this moment needs to be obtained in an implicit fashion to realize a large time step simulation. For the purpose of separating out the correction part, the following expansion formula is utilized [23]. The charge density is expanded in terms of a small displacement due to the correction electric field $\nabla\delta\varphi$,

$$\begin{aligned}\rho^{n+1}(\mathbf{x}) &= \sum_j e_j S(\mathbf{x}-\mathbf{x}_j^{n+1}) \\ &\cong \sum_j e_j S(\mathbf{x}-\mathbf{x}_{j(l)}^{n+1}) - \nabla\cdot\left(\sum_j e_j\delta\mathbf{x}_j S(\mathbf{x}-\mathbf{x}_{j(l)}^{n+1})\right). \end{aligned} \tag{32}$$

The displacement is defined by $\delta\mathbf{x}_j = \mathbf{x}_j^{n+1} - \mathbf{x}_{j(l)}^{n+1}$ with $\mathbf{x}_j^{n+1}$ being the true particle position at $t = t^{n+1}$, and $\mathbf{x}_{j(l)}^{n+1}$ the position calculated using the already known electromagnetic field $\breve{\mathbf{E}}^{n+1}$ and $\mathbf{B}^{n+1}$. The displacement of the ions, for example, is calculated to be

$$\delta\mathbf{x}_j^{(i)} = -\frac{1}{2}\alpha(\Delta t)^2\frac{e_i}{m_i}\{\nabla\delta\varphi + \nabla\delta\varphi\times\Theta\mathbf{b}^{n+\alpha} + \Theta^2\nabla_\parallel\delta\varphi\}/(1+\Theta^2), \tag{33}$$

where the vector operator is defined by $\nabla_\parallel = \mathbf{b}^{n+\alpha}\,(\mathbf{b}^{n+\alpha}\cdot\nabla)$. Since the final magnetic field has already been determined at this step together with $\breve{\mathbf{E}}^{n+1}$, the displacement $\delta\mathbf{x}_j$, hence the charge density ρ^{n+1}, is solely a function of $\delta\varphi$. By substituting Eq.(32) into Eq.(31) and shifting the $\delta\varphi$-dependent terms to the left-hand side, we obtain the equation to determine the correction scalar potential $\delta\varphi$,

$$\begin{aligned}\nabla^2\delta\varphi &+ \frac{1}{2}\alpha(\Delta t)^2\nabla\cdot\Big(\omega_{pi}^2(\mathbf{x})\{\nabla\delta\varphi + \Theta^2\nabla_\parallel\delta\varphi + \Theta\nabla\delta\varphi\times\mathbf{b}\}/(1+\Theta^2) \\ &\quad + \omega_{pe}^2(\mathbf{x})\,\nabla_\parallel\delta\varphi\Big) + 4\pi(-e)c\alpha\Delta t\,\nabla\cdot(\nabla\delta\varphi\times(\mathbf{b}/B)\,n_e(\mathbf{x})) \\ &= -4\pi\bar{\rho}^{n+1} + \nabla\cdot\breve{\mathbf{E}}^{n+1}. \end{aligned} \tag{34}$$

Here, $\bar{\rho}^{n+1}(\mathbf{x}) = \sum_j e_j S(\mathbf{x}-\mathbf{x}_{j(l)}^{n+1})$ and $\omega_{pj}^2(\mathbf{x}) = 4\pi n_j(\mathbf{x})e_j^2/m_j$. In Eq.(34) the vacuum response is mostly shielded by the plasma dielectric response. It is mentioned in passing that, in a two-dimensional plasma with an ambient magnetic field perpendicular to

the simulation plane, the major terms on the left-hand side are $\frac{1}{2}\alpha(\Delta t)^2\nabla\cdot(\omega_{pi}^2\nabla\delta\varphi)+4\pi(-e)c\alpha\Delta t\ \nabla\cdot(\nabla\delta\varphi\times(\mathbf{b}/B)\ n_e)$. The ion term, which is $(1/2)\omega_{ci}\Delta t$ times that of the electron term, must be numerically resolved in order to make the right correction to the electric field.

The procedures of the implicit-particle simulation described in this section are summarized in the Appendix. The particles are first generated in the Cartesian $(\mathbf{x},\mathbf{v})$ space. After collecting the current and charge densities, $\mathbf{j}^{(0)}$ and $\rho^{(0)}$, the initial electromagnetic field is determined. Using this magnetic field, the electron velocity is converted from the Cartesian to $(\mu, v_\perp, v_\parallel)$ representation. Then, a time cycle of the simulation begins, which is divided into two steps. Step I: For the future E/M field, solve the coupled field-particle equations in an implicit fashion. These equations are derived by combining the Maxwell and Newton-Lorentz equations. Step II: Push particles explicitly using the E/M fields calculated in Step I, and update particle informations.

In Step I, the current density $\mathbf{j}$ and the number densities n_i, n_e of the ions and electrons are summed up. The electromagnetic field $\breve{\mathbf{E}}^{n+1}$ and $\mathbf{B}^{n+1}$ are solved using the CCFP equation Eq.(25) and (21). Next, the charge density $\bar{\rho}$ and the particle number densities at the time $t=t^{n+1}$ are summed and the correction to the longitudinal part of the electric field is made using Eq.(34). Then, in Step II the velocity and position of all the particles are advanced by a full time step to proceed to the new time cycle.

2.4 Brief Notes on Numerical Techniques

Before closing this section, it is mentioned that advanced numerical techniques are required for solving the elliptic-type implicit equations. Also, it is essential to decouple the unknown electromagnetic field from the summations in the coupled field equation in order to make the whole scheme practical in actual simulations. The following accuracy-preserving formula is applied to the coupled equation,

$$\sum_j f_j\tilde{\mathbf{E}}^{n+\alpha}(\mathbf{x}_j)S(\mathbf{x}-\mathbf{x}_j) = \sum_j f_j\{\alpha(\tilde{\mathbf{E}}^{n+1}(\mathbf{x}_j)-\tilde{\mathbf{E}}_1(\mathbf{x}_j))+\tilde{\mathbf{E}}_0(\mathbf{x}_j)\}\ S(\mathbf{x}-\mathbf{x}_j) \quad (35)$$

$$\cong \alpha F(\mathbf{x})(\mathbf{E}^{n+1}(\mathbf{x})-\mathbf{E}_1(\mathbf{x}))+\sum_j f_j\tilde{\mathbf{E}}_0(\mathbf{x}_j)\ S(\mathbf{x}-\mathbf{x}_j) \quad (36)$$

where $\mathbf{E}_1$ is a quantity which is expected to well approximate $\mathbf{E}^{n+1}$ and $\mathbf{E}_0=\alpha\mathbf{E}_1+(1-\alpha)\mathbf{E}^n$. Using the above formula, Eqs.(25)-(27) given in Section 2.3(a) are rewritten

$$A(n_i,n_e;\mathbf{B}^{n+1})\ \mathbf{E}^{n+1} = \mathbf{S}(\mathbf{E}^n,\mathbf{B}^n;\mathbf{B}^{n+1}). \quad (37)$$

Here, the matrix A includes both the plasma and vacuum terms as defined by

$$\begin{aligned} A &= 1+(\alpha c\Delta t)^2(\nabla\nabla-1\nabla^2)+D \\ D &= (\alpha\Delta t)^2\left(\omega_{pi}^2(\mathbf{x})\{1-\Theta\mathbf{b}^{n+\alpha}\times 1+\Theta^2(\mathbf{bb})^{n+\alpha}\}/(1+\Theta^2)\right. \\ &\quad \left.+\omega_{pe}^2(\mathbf{x})(\mathbf{bb})^{n+\alpha}\right)-4\pi(-e)c\alpha\Delta t\ (n_e(\mathbf{x})/B)\ \mathbf{b}^{n+\alpha}\times 1, \end{aligned} \quad (38)$$

where (bb) is a dyadic tensor and $\omega_{pj}^2(\mathbf{x}) = 4\pi n_j(\mathbf{x})e_j^2/m_j$. The future electric field $\mathbf{E}^{n+1}$ is removed from $\mathbf{S}_p$ to obtain the new source vector

$$\begin{aligned}\mathbf{S} \;=\; & [1-\alpha(1-\alpha)(c\Delta t)^2(\nabla\nabla-\nabla^2)]\;\mathbf{E}^n + c\Delta t\;\nabla\times\mathbf{B}^n \\ & + D\mathbf{E}_\mathrm{i} \;-\; 4\pi\Delta t\;\{\sum_{j=i} e_i\;[\mathbf{v}_j^n + \alpha\Delta t(e_i/m_i)\left(\tilde{\mathbf{E}}_0 + \frac{\mathbf{v}_j^n}{c}\times\tilde{\mathbf{B}}^{n+\alpha}\right) \\ & \qquad /(1+\Theta^2)]\;S(\mathbf{x}-\bar{\mathbf{x}}_j^{n+\alpha}) \;+\; \cdots\cdots\}. \qquad (39)\end{aligned}$$

When $\mathbf{E}_\mathrm{I}$ is chosen independently of the iteration which is executed to solve the coupled field-particle equations, the summations in Eq.(39) need to be calculated only once before the commencement of the iteration.

A large set of algebraic equations thus derived is solved with aid of a bi-conjugate gradient (BCG) method [25]. In the BCG matrix solver, a recursive solution converges steadily to the final solution which is to be obtained in a finite number of iterations. Practically, a convergence of the BCG solver depends on the method of preconditioning the original matrix. A block-type BCG solver prescribes the 3×3 *core matrix* elements simultaneously as a block; the core matrix corresponds to the diagonal element $\Psi_{ijk} = (E_x, E_y, E_z)_{ijk}$. On the other hand, a scalar-type solver preconditions each row of the matrix separately. The block-type solver converges much better than the scalar-type one when the skewed symmetric elements of the core matrix, which arise from the $\mathbf{E}\times\mathbf{B}$ drift, are predominant over the diagonal elements. The accuracy of the solution obtained by the BCG method is quite satisfactory, and, therefore, the reliability of the nonlinear Ψ-iteration and the simulation itself have improved dramatically (Section 4).

Finally, for the choice of the time-decentering parameter α and its consequence on the energy conservation, refer to Reference [14].

2.5 Measurement of MHD Eigenmodes in 2-D Plasmas

The implicit particle code HIDENEK described in Section 2 is examined by measuring the MHD eigenmodes in a two-dimensional homogeneous plasma [7]. Initially, the ions and electrons are loaded randomly in space; in the velocity space they follow the Maxwell distributions of given temperatures. The simulation system is periodic both in the x and z-directions with an ambient magnetic field applied in the z-direction. The parameters are $\omega_{ce}/\omega_{pe} = 1$, $\beta_e = 0.04$, $T_i/T_e = 1$ and $m_i/m_e = 100$. A simulation run is performed during which the electric and magnetic field data are sampled. After the run, those data are Fourier analyzed to obtain the dispersion diagram in the $\omega - k$ space.

Figure 1 shows the dispersion relation for (a) parallel propagation, and (b),(c) perpendicular propagation. The magnetic perturbations are used for panels (a) and (b), and the electric perturbation for (c). The ordinates in the figures are the frequency ω/ω_{pe} and the abscissas are either the parallel wavenumber $ck_\parallel/\omega_{pe}$ or the perpendicular wavenumber

$ck_\perp/\omega_{pe}$. The power amplitude of the measured electromagnetic perturbations for given (k,ω) are plotted to the right of each baseline (fixed k value) in a logarithmic scale.

In Figure 1(a) of the parallel propagation, we can see two series of power spectrum peaks. One goes up to the higher end of the frequency in the diagram and the other levels off to the ion cyclotron frequency at $\omega_{ci}/\omega_{pe} = 10^{-2}$. An MHD-theory for the Alfven and whistler waves are shown with the solid and dashed lines in the figure. Agreement between the measurement and the theory is quite excellent. The dispersion relation for the perpendicular propagation is shown in Figure 1(b). This time, we have only one eigenmode which is the fast magnetosonic wave. The theoretical value is shown with the solid line. The agreement is again excellent. Shown in Figure 1(c) is the case of oblique propagation. The upper eigenmode corresponds to the fast magnetosonic wave, and the lower one to the kinetic Alfven wave [4]. The eigenmode branch of the kinetic-Alfven wave looks faint because this is a damped wave due to electron Landau damping.

3. The Electromagnetic Ion Beam-Plasma Instability

The first application of the closely-coupled implicit method to the low-frequency nonlinear plasma phenomena is a one-dimensional simulation of the electromagnetic ion beam-plasma instability. When a tenuous ion beam propagates along the ambient magnetic field through a dense background plasma in a velocity faster than the Alfven speed v_A, the electromagnetic ion-ion beam-plasma instability is excited [26]. The instability was investigated in connection with the diffused solar wind ions reflected from the earth's bow shock. A hybrid-particle simulation with particle ions and massless electrons was performed to find the origin of these ions [27].

The dispersion equation for the electromagnetic ion beam-plasma instability is given by [26,27]

$$\omega^2 - c^2k^2 + \sum_j \omega_{pj}^2 \frac{\omega - kV_{dj}}{kv_j} Z\left(\frac{\omega - kV_{dj} + \omega_{cj}}{kv_j}\right) = 0, \tag{40}$$

where $\omega_{pj} = (4\pi n_j e_j^2/m_j)^{1/2}$, $\omega_{cj} = e_jB/m_jc$ are the plasma and cyclotron frequencies of the j-th species, respectively. $Z(\xi)$ is the plasma dispersion function, $v_j = (2T_j/m_j)^{1/2}$ the thermal speed and V_{dj} is the drift velocity along the ambient magnetic field. There are two unstable roots to Eq.(40) which are either resonant ($kV_d > 0$) or nonresonant ($kV_d < 0$). The resonant mode has a larger growth rate and its typical frequency, growth rate and wavenumber in the $V_d/v_A \gg 1$ and $n_b/n_0 \ll 1$ limit are $\omega_r/\omega_{ci} \sim 0.2$, $\omega_i/\omega_{ci} \sim (n_b/2n_0)^{1/3}$ and $kV_d/\omega_{ci} \sim 1$, respectively, where n_b is the density of the beam ions.

Formerly, the hybrid simulation with particle ions and massless electrons used to be a major tool of simulating the low-frequency electromagnetic waves and instabilities. Implicit assumptions behind the hybrid simulations are (1) the quasi charge-neutrality of the plasma, (2) no electron orbit effects, and (3) instantaneous relaxation (adjustment) of the

electrons. Since the electron inertia and orbit motions are ignored, particle and energy transport of the electrons along the magnetic field is beyond the scope of the hybrid simulation. This situation occurs, for example, in the parallel shocks where the electrons are allowed to move freely along the magnetic field. By contrast, in the closely-coupled implicit method, the electrons are treated as independent particle species so that their relaxation along the magnetic field is naturally taken into account.

The parameters chosen in the HIDENEK simulation are the ion beam speed $V_d = 10v_A$, the beam density $n_b/n_0 = 0.015$, the ambient magnetic field strength $\omega_{ce}/\omega_{pe} = 10^{-3}$, and the electron plasma beta $\beta_e = 8\pi n_e T_e/B^2 = 1$ [28]. The electron and ion temperatures are the same, $T_i/T_e = 1$. The system is periodic along the ambient magnetic field (z-direction) with the length $L_z = 2560c/\omega_{pe}$ and 128 space grids. The mass ratio is $m_i/m_e = 100$ and the number of particles for each species is 16,384. The time step is $\omega_{pe}\Delta t = 2500$. The decentering parameter is $\alpha = 0.6$. A numerical filter is not applied. These parameters correspond to $\omega_{ci}\Delta t = 2.5 \times 10^{-2}$, $v_e\Delta t/\Delta z \cong 0.13$, and $\Delta z/\lambda_e \cong 3 \times 10^4$ with $\lambda_e = v_e/\sqrt{2}\omega_{pe}$ being the Debye length.

Figure 2 shows the time histories of the perturbed magnetic field energy, the kinetic energies of the beam and background ions, and the parallel kinetic energy of the electrons. The instability grows exponentially and the magnetic field energy peaks around $\omega_{ci}t \sim 70$. The electric field energy is roughly $(v_A/c)^2$ times that of the magnetic field energy. Later the magnetic energy decays to a quarter level compared to the primary peak, and small peaks follow the primary one periodically. Large decrease in the beam kinetic energy occurs in coincidence with the growth of the instability. The background ions are heated roughly by 20 percents, but the electrons are hardly affected. As is found by comparing Figure 2(a)-(c), the beam kinetic energy is mainly converted to the magnetic energy and to some extent to the background ions at the growth of the instability and vice versa during the relaxation oscillations.

The large decrease in the kinetic energy of the beam ions is attributed to the decrease in the drift speed (Figure 3(a)). Except for a temporary recovery of the beam speed at $\omega_{ci}t \sim 90$, the beam speed continues to decrease. This reveals that a part of the drift energy irreversibly goes to the thermal energy of both the beam and background ions. Conservation of the total energy slightly degrades at the growth of the instability. However, the total energy deviates by 5% during the saturation of the instability and it recovers to within 2% in the later times.

The electromagnetic field at the saturation time of the instability $\omega_{ci}t = 80$ is shown in Figure 4. The observed wave that is excited by the instability is circularly polarized and is consistent with the linearly most unstable mode ($m = 4 \sim 5$) of the electromagnetic ion beam-plasma instability. The electric field looks somewhat jagged because the numerical filter has not been applied. But, the phase relation between the corresponding pairs of the electromagnetic field looks fine, *i.e.*, $B_x \sim -E_y$, $B_y \sim E_x$. The frequency and the growth

rate are measured to be $\omega/\omega_{ci} \cong 0.22 + 0.15i$ for the mode $m = 5$ which are in reasonable agreement with the theoretical value $\omega^{th}/\omega_{ci} = 0.23 + 0.19i$.

The nonlinear behavior of the beam ions is shown in the particle scatter plots of Figure 5. The ions sitting initially around $V_d = 10v_A$ (Figure 5(a)) are significantly affected by the instability as shown in Figure 5(b) for $\omega_{ci}t = 80$. Obviously, the average beam speed has drastically decreased. When viewed in the $(v_z, v_\perp)$ space, the beam ions are scattered in the pitch-angle; they finally become equally distributed along the arc whose center is located on the $v_\perp = 0$ axis at $(v_A, 0)$. Formation of the equally distributed arc is clearly seen at $\omega_{ci}t = 200$ in Figure 5(c). As noted previously, the electrons behave almost adiabatically. Although the electrons carry substantial $E \times B$ current in the perpendicular direction, they are hardly affected and heated by the instability simply because the wave frequency is by orders of magnitude smaller than the electron cyclotron frequency, $\omega/\omega_{ce} \ll 1$.

Before closing this section, a comparison of the present results with those of other implicit and hybrid particle codes is briefly made. The difference between the HIDENEK and CELEST codes is that the former chooses the magnetic field $\mathbf{B}^{n+\alpha}$ in the equations of motion and optionally the guiding-center approximation to the electrons, whereas the fully kinetic electrons and $\mathbf{B}^n$ are used in the latter [13]. The hybrid simulation requires artificial viscosity to control (damp out) spiky oscillations in the perturbed magnetic field, especially when the ambient magnetic field lies close to the simulation plane [27], which makes the simulation results somewhat artificial. Despite these differences, the growth and saturation of the instability and associated nonlinear results such as scattering of the beam ions and decrease in the beam drift speed have agreed generally well among the three simulations of the electromagnetic ion beam-plasma instability. The detailed comparison will be made elsewhere.

4. The Kink Instability in the Three-Dimensional Space

The most challenging and stringent test of the HIDENEK code will be a simulation of low-frequency instabilities which occur in the finite-beta, inhomogeneous plasmas of the three-dimensions. The diamagnetic particle drift and magnetization currents are important to maintain the pressure-balanced plasma profile. Moreover, in the three-dimensional space, the $E \times B$ drift works in a subtle way so that it causes a motion of charged particles across the magnetic field leading to a coupling of electrostatic and electromagnetic components of the electric field.

A three-dimensional simulation of the Alfven critical current [29] for the relativistic electron beam was carried out previously by using the semi-implicit version of the closely-coupled implicit method; the kink instability was observed there [21]. In this section, the closely-coupled implicit method described in Section 2 is applied to the kink instability of the current-carrying beam which has an inhomogeneous peaked-density profile.

The simulation is performed in the Cartesian space (x, y, z, v_x, v_y, v_z). The size of the

simulation box is $L_x = L_y = 100c/\omega_{pe}$ and $L_z = 2000c/\omega_{pe}$ with $27 \times 27 \times 32$ grids. The x and y-directions are limited by conducting walls and the both ends of the z-direction are periodically connected to each other. The average number of super-particles per cell is sixteen for each of the electron and ion species, which amounts to 320,000 electrons and ions, respectively. The initial plasma has a bell-shaped density profile, $n_0(r) \sim \exp[-(r/L_n)^2]$, with $L_n = 37c/\omega_{pe}$ where r is the radial distance from the center of the poloidal (x, y) plane. There is a vacuum region between the plasma and the wall. The constant magnetic field is applied in the z-direction along which a drift velocity is given to the ions to maintain the peaked, inhomogeneous plasma profile by the magnetic pressure. The drift speed and the plasma temperatures must be consistently chosen so that the pressure balance $n(T_e + T_i) + B^2/8\pi = const.$ be satisfied radially. Otherwise, a rapid pinch (or expansion) of the initially-loaded plasma results in the finite-beta plasma simulation.

Other parameters are the ambient magnetic field strength $\omega_{ce}^{(0)}/\omega_{pe} = 1$, the temperature ratio $T_e/T_i = 1$ and the electron beta value $\beta_e = 8\pi\bar{n}_e T_e/B^2 = 0.04$. The mass ratio is $m_i/m_e = 400$ and the time step is $\omega_{pe}\Delta t = 100$ (*i.e.*, $\omega_{ci}\Delta t \sim 0.25$). The implicitness parameter is $\alpha = 0.6$. The safety factor of the plasma, which is the ratio of the number of toroidal rotation of the magnetic field line to that of its poloidal rotation, becomes $q^{(0)}(r) \approx 0.6$ at the radial distance $r = L_n$. Thus, a helical rotation is initially present in the magnetic field structure (not in the current). By contrast to one-dimensional simulations in Section 3, a digital filter is introduced to smooth the source terms of the CCFP equations. The digital filter helps to reduce the fluctuating electric field level arising from a grid-to-grid scale charge separation of plasma particles for which the finite spatial-differencing does not have a correct resolution. The weight of sampling for the consecutive five points along one direction is $(-1/16, 4/16, 10/16, 4/16, -1/16)$ (cf. Appendix of [5]) and the digital filter is applied once to each direction in a tri-linear fashion .

The simulation run has been continued up to $\omega_{pe}t = 2.6 \times 10^4$ or $t = 3.5\tau_A$. Here, the poloidal Alfven time is defined by $\tau_A = 2L_n/v_{Ap} \sim 7.4 \times 10^3 \omega_{pe}^{-1}$ with $v_{Ap} = B_p/(4\pi m_i n)^{1/2}$ being the poloidal Alfven speed. The time history of the magnetic field energy is shown in Figure 6(a) (the constant part $(B_0)^2$ has been omitted). A sudden increase in the magnetic field energy takes place at the beginning of the simulation. This is a self-adjustment of the beam-plasma system because the initial current flows in the z-direction which is not exactly along the helical magnetic field. The magnetic field energy increases gradually to $t = 3.5\tau_A$. The electric field energy is dominated by the component due to the radial electric field which appears to be almost independent of the instability. The ion kinetic energy in Figure 6(b) increases slightly during the simulation which is attributed to an increase in the perpendicular temperature. On the other hand, the electron kinetic energy decreases monotonically which arises from a decrease in the parallel temperature. This is considered to be an artificial cooling caused by incomplete Debye shielding. The total

energy of the system deviates about ±5% during the simulation as shown in Figure 6(d).

The cross-sectional plots of the current and charge densities of the ions at the mid-plane ($y = L_y/2$) are shown in Figure 7 for (a) $t = 0.27\tau_A$ and (b) $t = 3.2\tau_A$. The left-hand side panels correspond to the early state after the initial transient motions have subsided. In the right-hand side panels, we can see a deformation of the beam current which is projected to the toroidal mid-plane. The dominant mode number of the deformation in the z-direction is found to be n=1. The whole aspect of the deformation of the beam current is better observed in the bird's-eye-view scatter plots of ions and electrons in Figure 8. The top panel is the plot for the ions at $t = 0.27\tau_A$ and the middle and bottom panels show the ion and electron species at $t = 3.2\tau_A$, respectively. Almost the same spatial distortions are observed both in the electrons and ions. Here, it is found that the aforementioned deformation is a helical perturbation which is occurring in the three-dimensional space.

Figure 9 is a hodogram plot of the location of the beam center. The toroidal direction is divided to eight bins and the positions of the ions (x_j, y_j) in each bin are averaged. The number i in the figure is the bin number corresponding to the z-position $z = iL_z/8$. The center of the circle in the figure coincides with that of the poloidal cross section and its radius is $3.5c/\omega_{pe}$. It is seen that, except a strayed and slow movement around 8-1-2, the beam axis rotates in the clockwise direction toward the positive z-direction. This helical pitch is the same as that of the initial magnetic field. The mode number of the helical distortion of the beam axis is determined to be m/n=1/1.

The poloidal component of the magnetic field is shown in the consecutive poloidal cross-sectional plots at $t = 3.2\tau_A$ (Figure 10). The toroidal separation between the two adjacent cross-sections is $\frac{1}{4}L_z$. The center of the magnetic axis (null point of the poloidal magnetic field) is seen to shift in the poloidal cross-sections. Plotting the locations of the magnetic axis, as we did for the beam axis, again shows a clockwise rotation of the magnetic axis toward the z-direction. By considering the plasma geometry used in the simulation and the fact that the helical deformation of the beam and magnetic field has occurred in a few poloidal Alfven times, we can conclude that the present instability is the ideal (external) kink instability [30].

5. The Kelvin-Helmholtz Instability and Plasma Mixing

It has been suggested that the Kelvin-Helmholtz (KH) instability plays an important role in the boundary layer of the planetary magnetosphere [31,32] and edge plasmas of a tokamak [33]. Recent calculations using a hybrid-particle simulation code (particle ions and massless electron medium) suggest that the KH instability is responsible for anomalously fast ion mixing [34,35]. In this section, early simulation results of the KH instability using an implicit particle simulation method [13,14] are described, where a special emphasis will be placed on the kinetic effects to the saturation of the instability and associated particle /

energy transport across the magnetic field.

The implicit-particle model, in contrast to the hybrid-particle model, includes particle electrons as well as particle ions. The implicit formulation allows us to simulate a plasma with large time-and-space scales, $\Delta t \gg \omega_{pe}^{-1}$ and $\Delta x \geq c/\omega_{pe}$ ($\gg \lambda_{De}$), while keeping electron kinetic effects. The guiding center approximation to the perpendicular motion of the electrons, as shown in section 2, further permits $\Delta t \gg \omega_{ce}^{-1}$ [14].

The simulation is performed for a two-dimensional magnetized plasma [36]. The plasma is nearly homogeneous, and is bound by conducting walls in the x-direction and periodic in the z-direction. There is an initial sheared plasma flow in the z-direction, $V_0(x)$, which is sustained by a $\mathbf{E}_0(x) \times \mathbf{B}_0$ drift. This electric field, $E_0\hat{x}$, is due to a slight difference in the charge densities between the ions and electrons. The following simulation results are for the MHD-like parameter $\rho_i/a \cong 0.1$, with ρ_i the ion Larmor radius and a the width of the velocity-shear layer. The ambient magnetic field points the y-direction unless otherwise specified.

Figure 11 shows the time history of the electromagnetic field energies. The electric field energy E_z^2, which corresponds to the growth of the KH instability perturbation, increases during $(v_0/a)t = 0 - 15$ (v_0: shear velocity). When E_z^2 of an early time interval is plotted in a logarithmic scale, a clear exponential growth of the instability is observed. The line in the figure shows the linear theory for KH instability which very well fits the simulation result. As will be shown later, the fact that the electric field perturbation energy is kept in a comparatively high level during the entire nonlinear stage is important for plasma mixing. On the other hand, the sum of the total electric field energy E^2 suddenly starts to decrease at $(v_0/a)t = 20$ when the instability gets saturated. Since this energy mainly reflects the magnitude of the "radial" space-charge electric field E_x, the decrease means a relaxation of the velocity-shear layer in the x-directions.

Two-dimensional snapshots of the electric field (E_x, E_z) and the ion and electron current densities are shown in Figure 12 for $(v_0/a)t = 0, 19.2$ and 30.0. The scalar potential Ψ in the second panel is calculated from the electric field data of the top panel by $\mathbf{E} = -\nabla\Psi$. As the instability grows as was shown in Figure 11, a few vortex eyes of the KH instability are seen to develop within the shear layer for the scalar potentials of Figure 12(b). An inspection of the particle trajectories reveals that the plasma particles are pulled in, rotate along the scalar potential equi-contours of the vortices to migrate to the other side of the shear layer. In the late stage of the instability, the relaxation of the velocity-shear layer is found where the layer expands outward to nearly four times that of the original width of the layer (Figure 12(c)). This was observed as the decrease in the total electric field energy E^2 in Figure 11.

Mixing of the plasma particles with different spatial origins is measured. The definition of the mixing is the following: At $t = 0$, particles residing in the upper region $\{x \geq a\}$ are marked red, while the other particles in the lower region $\{x \leq -a\}$ are marked green.

Then, we sample particles from a specific cell at a later time, and if the population of both the red and green particles exceeds 25% of the total number of particles in that cell, we define that cell "mixed." Figure 13 shows a development of plasma mixing. As time goes on in the nonlinear stage of the KH instability, the mixed cells occupy the regions encircling the scalar potential vortices which have been formed by the instability.

The plasma mixing rate is quantitatively shown in Figure 14 for ions and electrons. Here, the ordinate is the number of mixed cells divided by the number of cells in the shear layer of thickness a. It is found that the plasma mixing develops in the same degree for the ions and electrons, probably due to choice of the MHD-like parameter $\rho_i/a \cong 0.1$. Also, it is found that the mixing goes linearly in time which continues during the entire period of the nonlinear stage. At the beginning of the mixing, on the other hand, there appears a t^2-phase which smoothly turns into the linear (t-) phase due to excitation of multi-modes in the present simulation.

A very striking discovery is that the (electrostatic) KH instability is confined to the plane perpendicular to the ambient magnetic field. When a simulation is performed with a slightly inclined ambient magnetic field $(0, B_0 \sin\theta, B_0 \cos\theta)$ with $\theta = 10°$, the growth of the electric field perturbation is not observed during the simulation with the other parameters remaining the same [36]. This phenomenon is considered to be due to the electron dynamics parallel to the ambient magnetic field. In fact, the parallel wavenumber is small but finite in this run, *i.e.*, $\mathbf{k} \cdot \mathbf{B}_0 \neq 0$. A linear theory implies that the present stabilization is due to the electron Landau damping when the parallel wavenumber is finite [37].

Finally, it is mentioned that the present simulations were performed in a collisionless plasma condition. Thus, the plasma mixing that was observed here does not lead to a complete mixing in microscopic spatial scales. However, once the two plasma elements with different origins come close enough and their orbits overlap with each other within the resolution of the simulation, they are regarded to be mixed. Further mixing will be caused by diffusion of their guiding centers owing to micro-turbulence which is expected to prevail in thermally non-equilibrium plasmas. Rather, the mixing which is targetted in the present simulations is a global phenomenon that occurs through finite Larmor radius effects of plasma particles.

Appendix: Procedures of the HIDENEK Simulation

The procedures that constitute one time cycle of the simulation are summarized. The upper part of the chart shows the initial loading of the plasma particles and the electromagnetic field. The lower part shows one time cycle of the simulation.

Initial loading of particles and fields

- Generate particles in (x, y, z, v_x, v_y, v_z) space.
- Accumulate $\mathbf{j}^{(0)}$ and $\rho^{(0)}$.
- Calculate initial electromagnetic field.
- Conversion of electron velocity: $(v_x, v_y, v_z) \rightarrow (\mu, v_\perp, v_\parallel)$.

Start of the time cycle

- Accumulate $\mathbf{j}$, n_i and n_e of $t = t^{n+\alpha}$.
- Solve the CCFP equation Eq.(25) for $\breve{\mathbf{E}}^{n+1}$ and $\mathbf{B}^{n+1}$.
- Accumulate ρ, n_i and n_e of $t = t^{n+1}$.
- Solve Eq.(34) for $\delta\varphi$ and correct $\breve{\mathbf{E}}^{n+1}$.
- Advance particles to $(\mathbf{x}^{n+1}, \mathbf{v}^{n+1})$.
- Plasma diagnosis

IF $t < t_{MAX}$, and (ctime) < $(\text{ctime})_{MAX}$, GOTO Start of the time cycle

END

Acknowledgements

The author is grateful to Professor J.U.Brackbill and Dr.H.X.Vu for fruitful collaborations on the implicit particle simulation since fall 1991. He thanks Professor K.Nishikawa for encouragements, Professor T.Sato and Dr.C.Z.Cheng for general discussions. Finally, he thanks the Yoshida Science and Technology Foundation (Tokyo) for supporting his travel of giving this lecture at the International Center for Theoretical Physics in Trieste.

References

1. B.Coppi, S.Migliuolo, F.Pegoraro and F.Porcelli, Phys. Fluids, B2, 927 (1990).
2. C.Z.Cheng, Phys.Fluids, B3, 2463 (1991).
3. G.R.Burkhart, J.F.Drake and J.Chen, J.Geophys.Res., 96, 11539 (1991).
4. A.Hasegawa and L.Chen, Phys. Fluids, 19, 1924 (1976).
5. C.K.Birdsall and A.B.Langdon, Plasma Physics via Computer Simulation, (McGraw-Hill, 1983).
6. Chapters 7-11 in Multiple Time Scales, edited by J.U.Brackbill and B.I.Cohen (Academic Press, 1985).
7. M.Tanaka, J.Comput.Phys., 79, 209 (1988).
8. W.W.Lee, J.Comput.Phys. 72, 243 (1987).
9. R.J.Mason, J.Comput.Phys., 47, 233 (1981).
10. J.Denavit, J.Comput.Phys., 42, 337 (1981).
11. J.U.Brackbill and D.W.Forslund, J.Comput.Phys., 46, 271 (1982).
12. D.W.Forslund and J.U.Brackbill, Phys.Rev.Lett., 48, 1614 (1982).
13. H.X.Vu and J.U.Brackbill, Comput.Phys.Comm., 69, 253 (1992).
14. M.Tanaka, J.Comput.Physics, vol.106 (1993), in press.
15. A.B.Langdon and D.C.Barnes, Chapter 11 in Multiple Time Scales (Academic Press, 1985).
16. D.W.Hewett and A.B.Langdon, J.Comput.Phys., 72, 121 (1987).
17. A.Friedman, J.Comput.Phys., 90, 292 (1990).
18. J.A.Byers, B.J.Cohen, W.C.Condit and J.D.Hanson, J.Comput.Phys., 27, 363 (1978).
19. M.M.Leroy, D.Winske, C.C.Goodrich, C.S.Wu and K.Papadopoulos, J.Geophys.Res., 87, 5081 (1982).
20. M.Tanaka, T.Sato and A.Hasegawa, Phys. Fluids, B1, 325 (1989).
21. M.Tanaka and T.Sato, Phys.Fluids, 29, 3823 (1986).
22. A.B.Langdon and B.F.Lasinski, Methods in Comput. Phys., 16, 327 (1976).
23. A.B.Langdon, J.Comput.Phys., 30, 202 (1979).
24. Private communication, J.U.Brackbill and H.X.Vu (1992).
25. H.Toda, The bi-conjugate gradient method (Kyoiku Pub., Tokyo 1990).
26. P.Gary, C.W.Smith, M.A.Lee, M.L.Goldstein and D.W.Forslund, Physics of Fluids, 27, 1852 (1984).
27. D.Winske and M.M.Leroy, J.Geophys.Res., 89, 2673 (1984).
28. This simulation uses the same parameters as those in Ref.12.
29. H.Alfven, Phys.Rev., 55, 425 (1939).
30. G.Bateman, MHD instabilities (MIT Press, 1978).
31. W.I.Axford and C.O.Hines, Can.J.Phys., 39,1433 (1961).
32. A.Miura, J.Geophys.Res., 89, 801 (1984).
33. R.G.Kleva and E.Ott, Physics of Fluids, 28, 941 (1985).

34. V.Thomas and D.Winske, J.Geophys.Res., submitted (1992).
35. T. Terasawa, M. Fujimoto, H. Karimabadi, and N. Omidi,
Geophys. Res. Lett., submitted (1992).
36. M.Tanaka and J.U.Brackbill, EOS Trans. (American Geophysical Union)
73, 459 (1992).
37. G.Ganguli, Y.C.Lee and P.Palmadesso, Physics of Fluids, 31, 823 (1988).

Measurement of eigenmodes in magnetized plasma

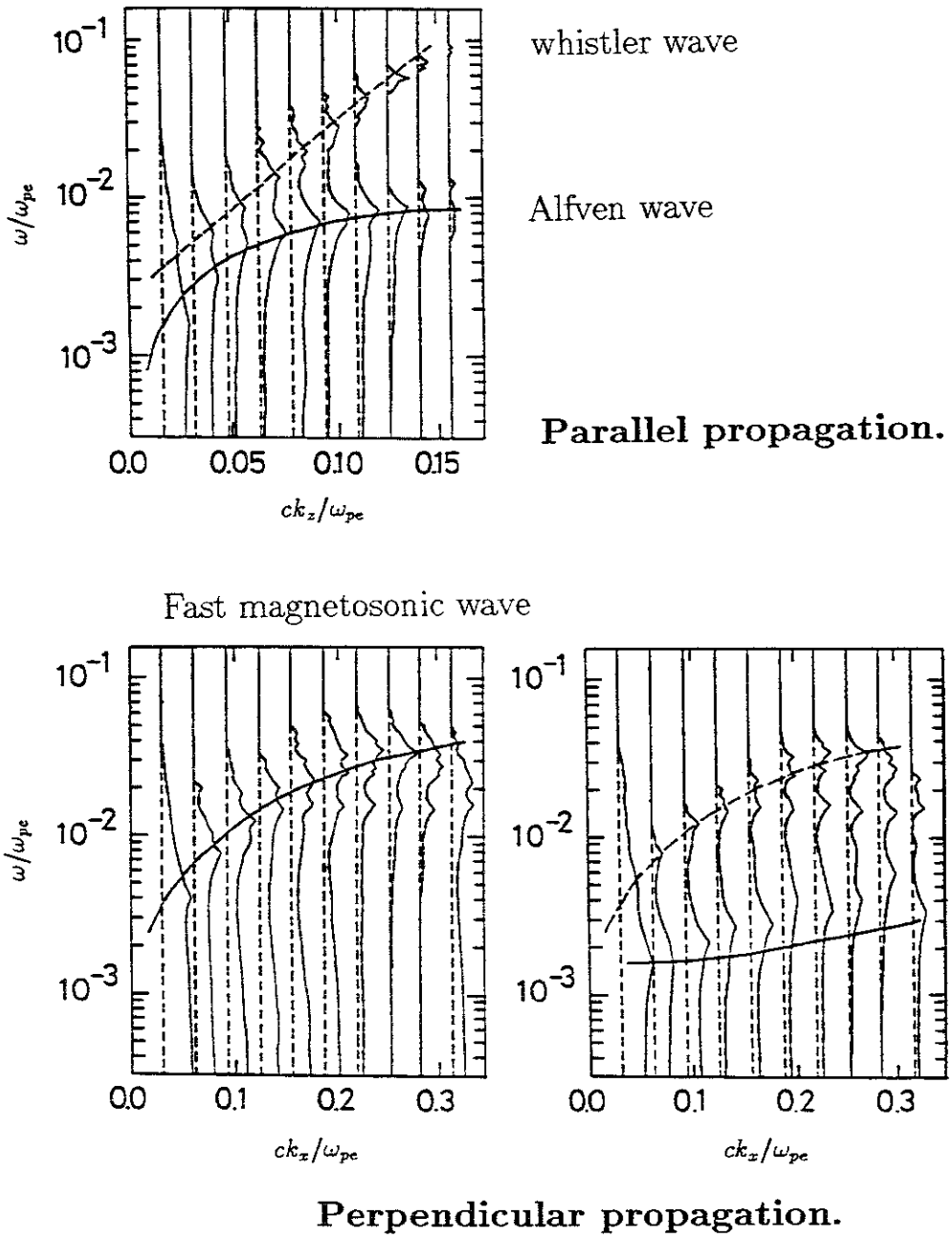

Figure 1. The measured eigenmodes in a two-dimensional homogeneous plasma. The panel (a) shows the eigenmodes for the parallel propagation, and (b)(c) for the perpendicular propagation.

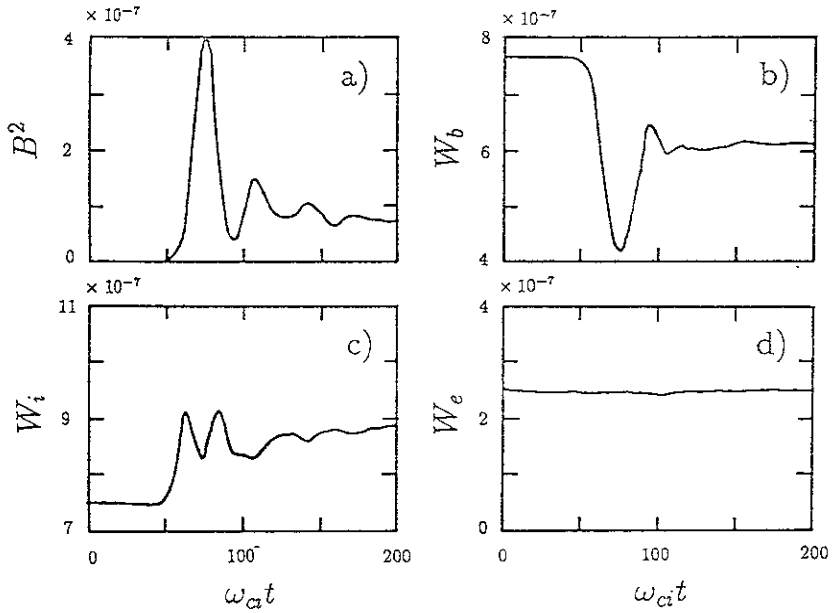

Figure 2. The time histories of (a) the perturbed magnetic field energy, (b)(c) the kinetic energies of the beam and background ions, respectively, and (d) the parallel kinetic energy of the electrons for the electromagnetic ion beam-plasma instability with $v_d/v_A = 10$ and $n_b/n_0 = 1.5 \times 10^{-2}$.

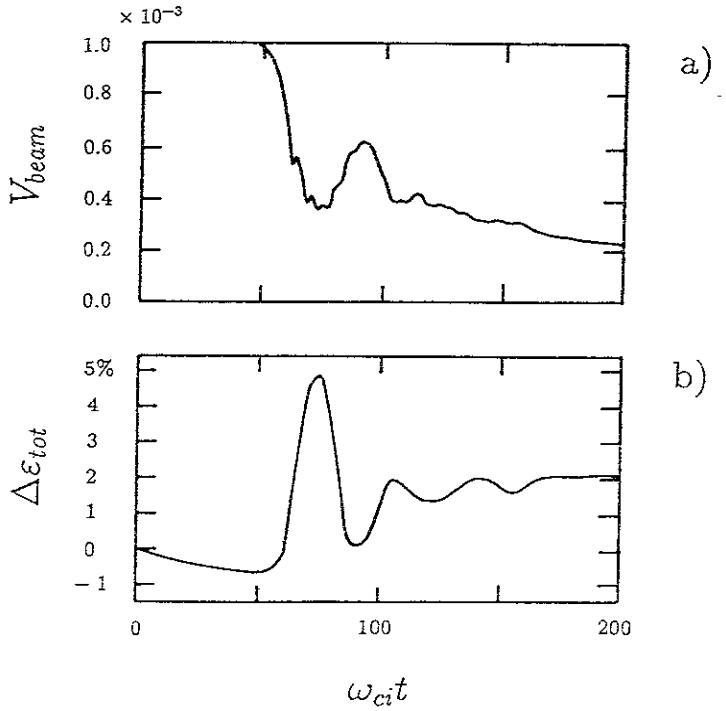

Figure 3. The time histories of (a) the average drift speed of the beam ions, and (b) the deviation of the system total energy in percent.

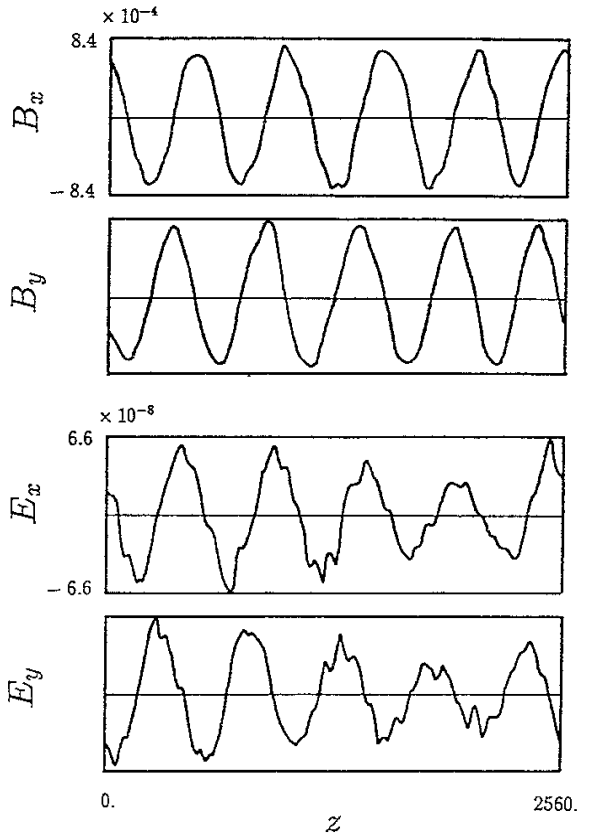

Figure 4. The electromagnetic field B_x, B_y, E_x and E_y at $\omega_{ci}t = 80$ from top to bottom, respectively.

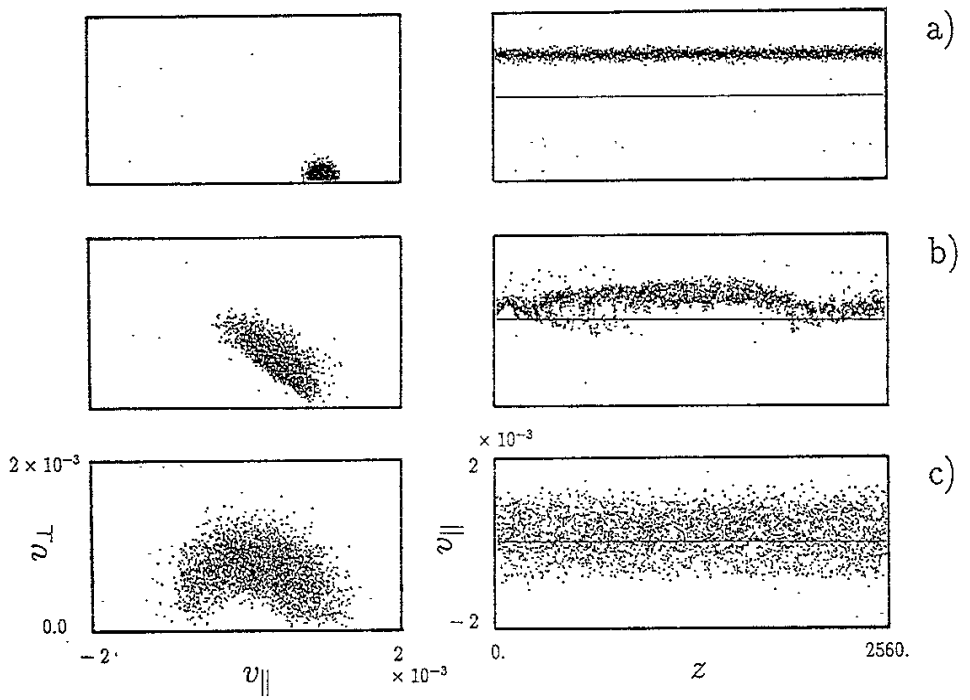

Figure 5. The distribution of the beam ions in the $(v_z, v_\perp)$ and (z, v_z) spaces in the left and right columns, respectively, for (a) $\omega_{ci}t = 0$, (b) $\omega_{ci}t = 80$, and (c) $\omega_{ci}t = 200$.

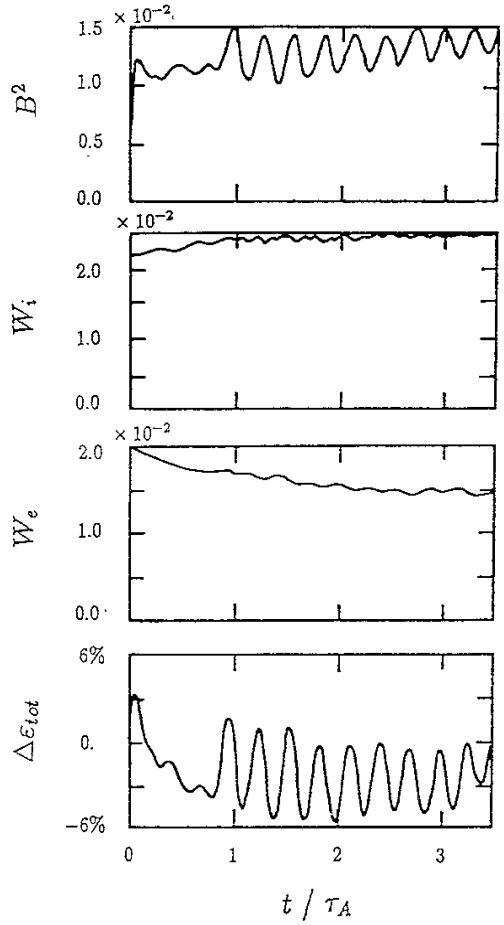

Figure 6. The time histories of (a) the magnetic field energy, (b) the ion kinetic energy, (c) the electron kinetic energy defined by $W_e = \frac{1}{2}m_e\bar{v}_{\|}^2 + \mu\bar{B}$, and (d) the deviation of the system total energy (the constant part $(B_0)^2$ is omitted in ε_{tot}).

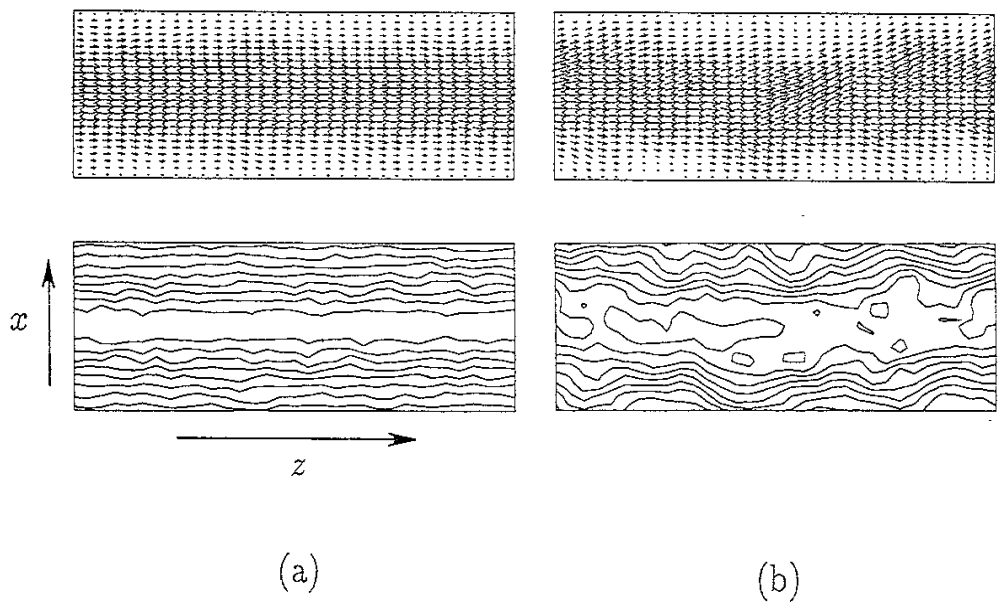

Figure 7. The cross-sections (at $y = \frac{1}{2}L_y$) of the current and charge densities in the upper and lower panels, respectively, at (a) $t = 0.27\tau_A$ and (b) $t = 3.2\tau_A$.

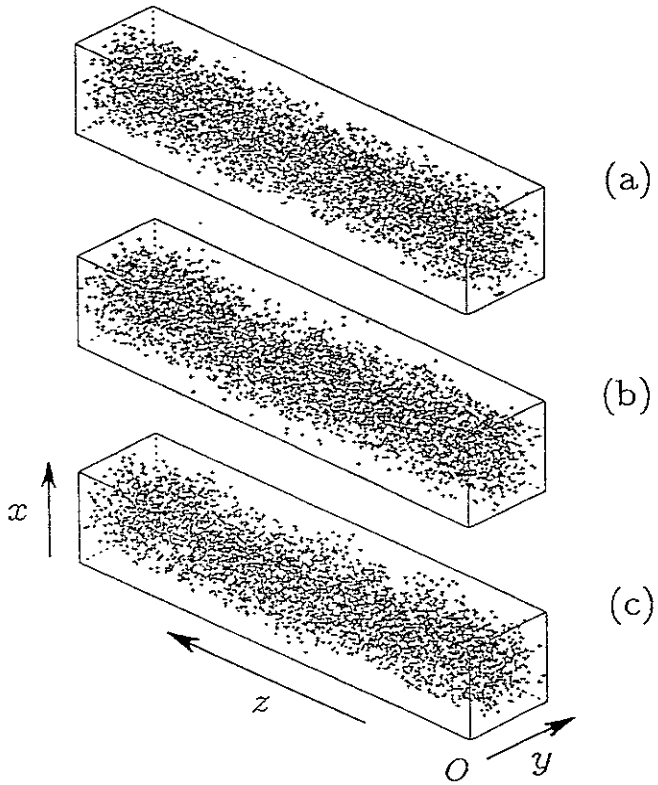

Figure 8. The bird's-eye-view scatter plots in the (x, y, z) space at (a) $t = 0.27\tau_A$ and (b)(c) $t = 3.2\tau_A$. The plots are for the ions except for the electrons in the bottom panel. The helical perturbation has the mode number m/n=1/1 (note the z-direction has been squeezed).

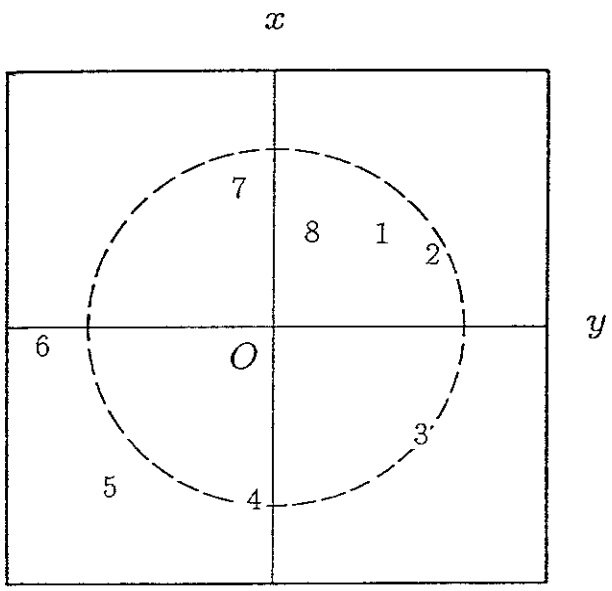

Figure 9. A hodogram plot of the beam axis locations at $t = 3.2\tau_A$. The number i shows the toroidal position $z = iL_z/8$.

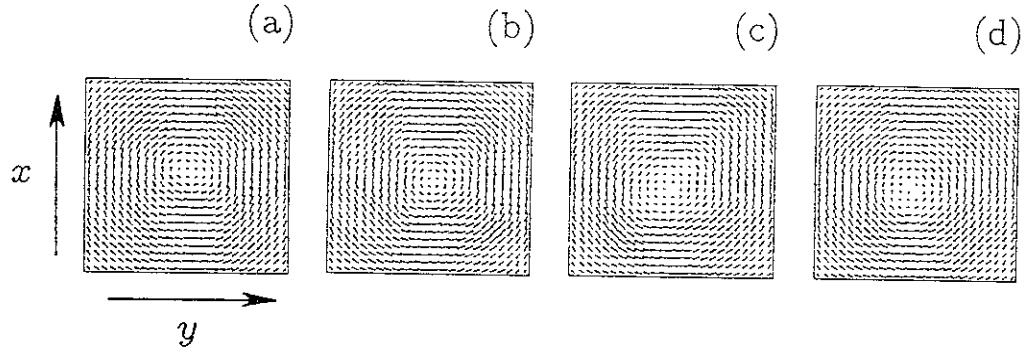

Figure 10. The poloidal magnetic field (B_x, B_y) in the consecutive poloidal cross sections (toroidal separation $L_z/4$) at $t = 3.2\tau_A$. The maximum amplitude of the poloidal magnetic field is 0.21 in the simulation unit.

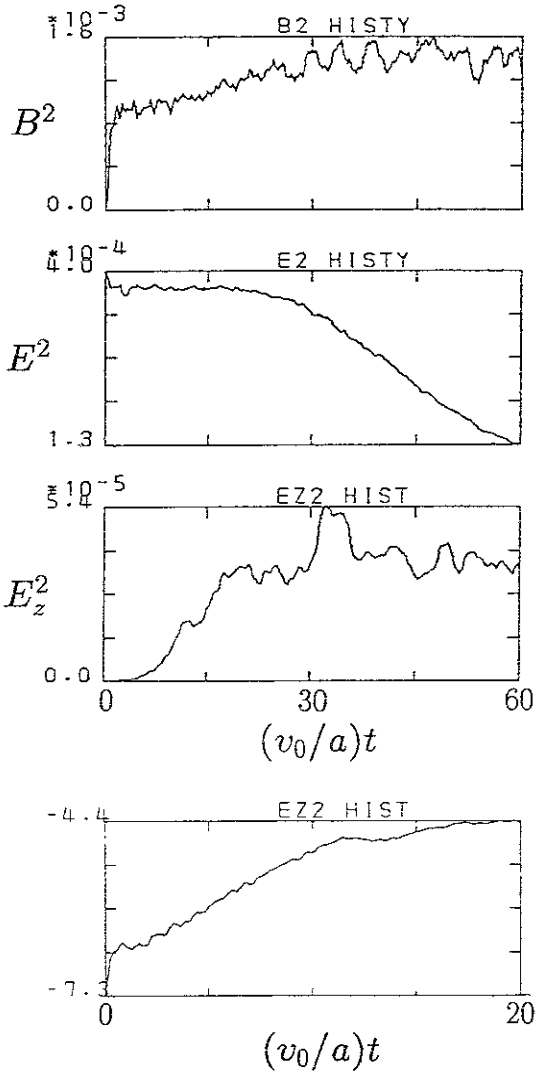

Figure 11. The time history of (a) the magnetic field energy, (b) total electric field energy, (c) the energy of the E_z electric field. The panel in (d) is a logarithmic plot of E_z^2 for $(v_0/a)t = 0 - 20$.

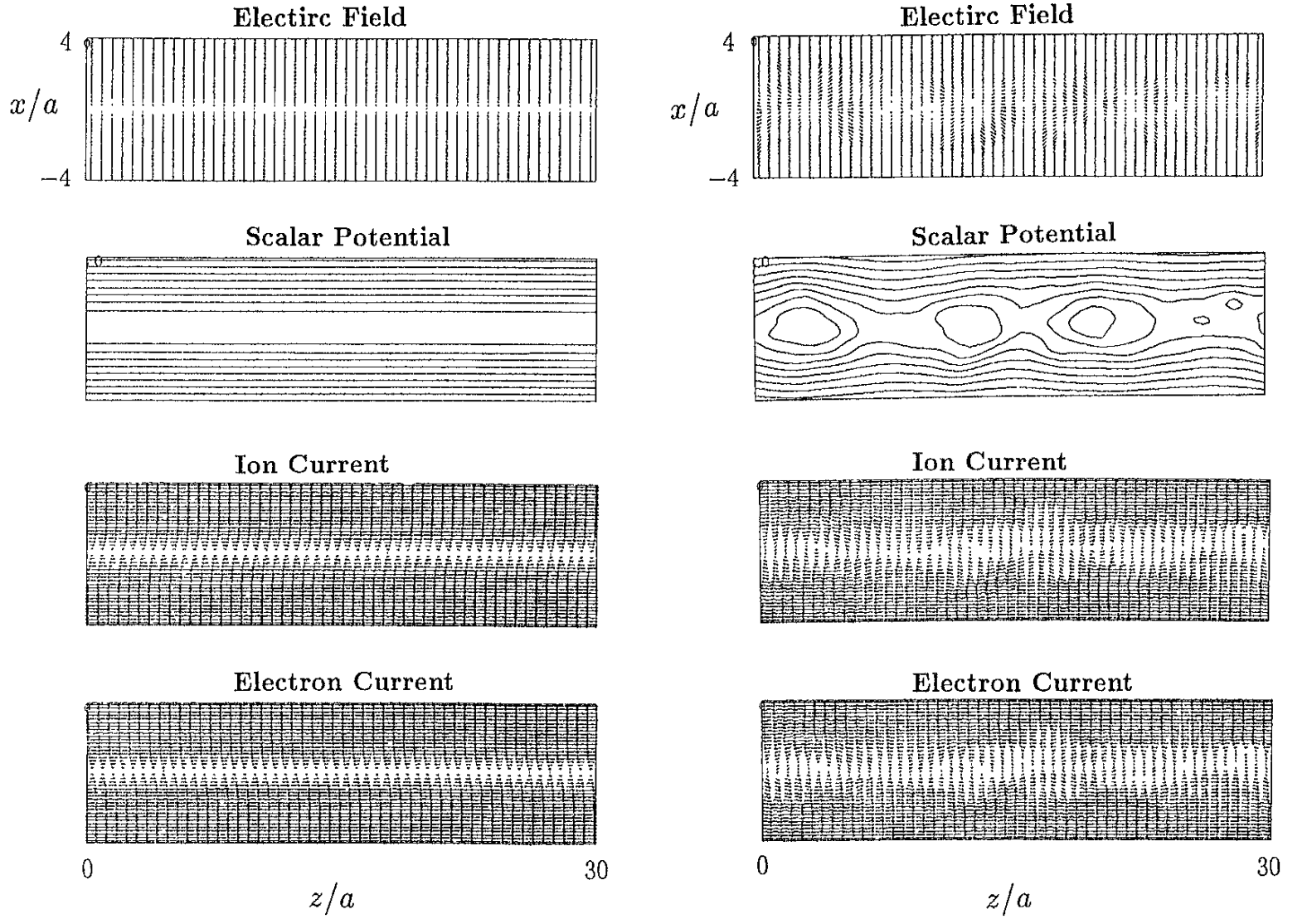

Figure 12. The snapshots of the electric field (E_x, E_z), the scalar potential Ψ, the ion and electron current densities for three different times of the run, (a) $(v_0/a)t = 0$, 19.2 and 30.0.

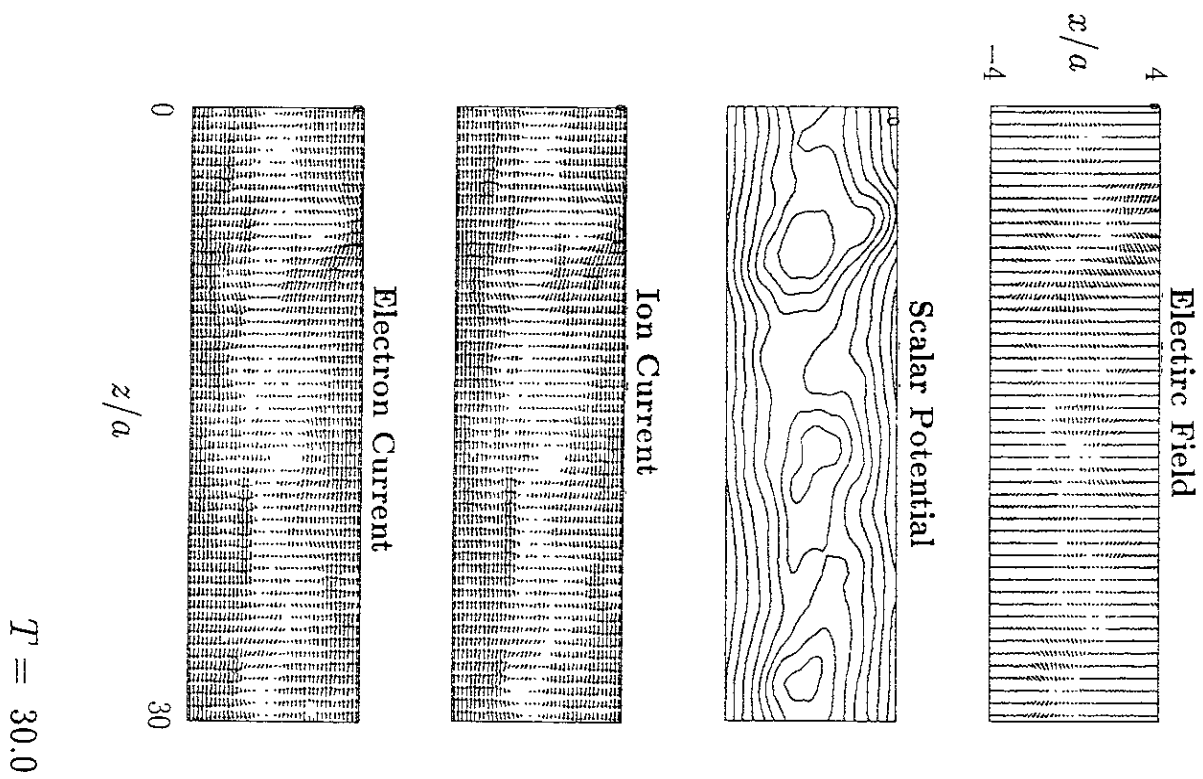

Development of Mixed Cells (Ions)

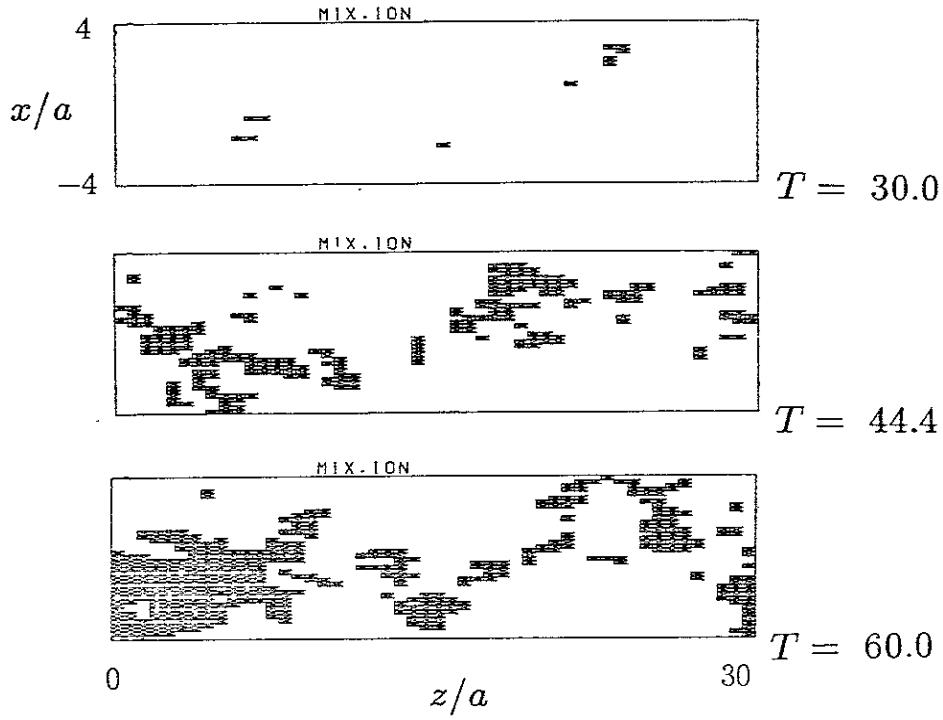

Figure 13. Development of "mixed" cells in the (x, z) plane in the nonlinear stage of the instability for $(v_0/a)t = 30 - 60$. The definition of the mixed cell is given in the text.

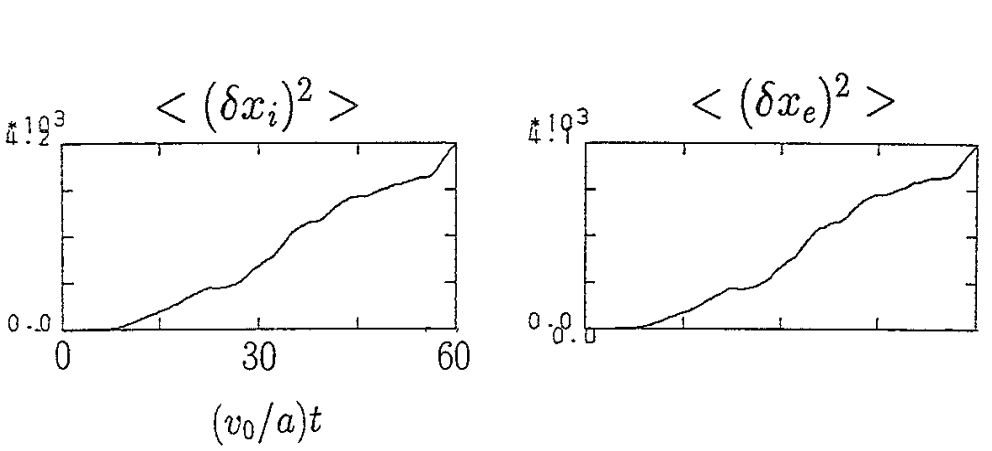

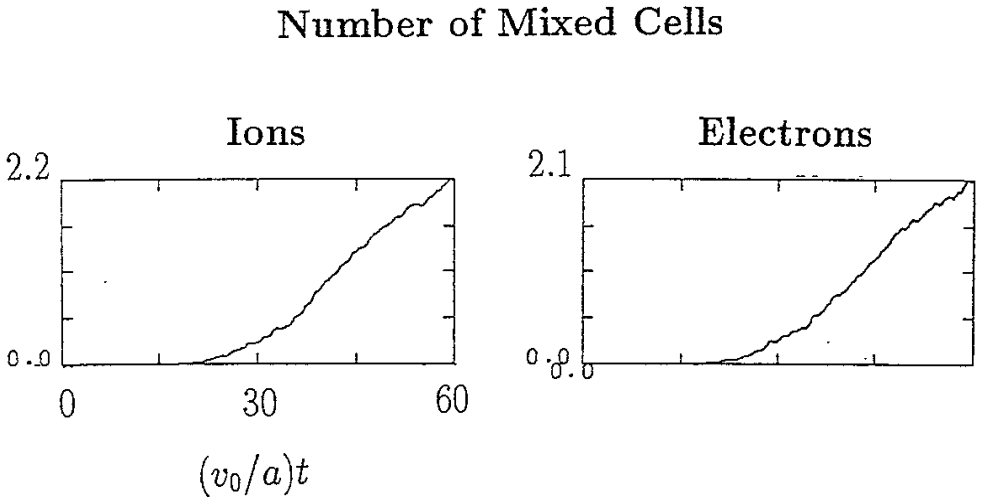

Figure 14. The time history of a number of the mixed cells for ions (left) and electrons (right). The plasma mixing occurs linearly in time during the nonlinear stage of the instability.

Recent Issues of NIFS Series

NIFS-180 H. Momota, Y. Tomita, A. Ishida, Y. Kohzaki, M. Ohnishi, S. Ohi, Y. Nakao and M. Nishikawa, *D-^{3}He Fueled FRC Reactor "Artemis-L"* ; Sep. 1992

NIFS-181 T. Watari, R. Kumazawa, T. Seki, Y. Yasaka, A. Ando, Y. Oka,O. Kaneko, K. Adati, R. Akiyama, Y. Hamada, S. Hidekuma, S. Hirokura, K. Ida, K. Kawahata, T. Kawamoto, Y. Kawasumi, S. Kitagawa, M. Kojima, T. Kuroda, K. Masai, S. Morita, K. Narihara, Y. Ogawa, K. Ohkubo, S. Okajima, T. Ozaki, M. Sakamoto, M. Sasao, K. Sato, K. N. Sato, F.Shimpo, H. Takahashi, S. Tanahasi, Y. Taniguchi, K. Toi, T. Tsuzuki and M. Ono, *The New Features of Ion Bernstein Wave Heating in JIPP T-IIU Tokamak* ;Sep, 1992

NIFS-182 K. Itoh, H. Sanuki and S.-I. Itoh, *Effect of Alpha Particles on Radial Electric Field Structure in Torsatron / Heliotron Reactor*; Sep. 1992

NIFS-183 S. Morimoto, M. Sato, H. Yamada, H. Ji, S. Okamura, S. Kubo, O. Motojima, M. Murakami, T. C. Jernigan, T. S. Bigelow, A. C. England, R. S. Isler, J. F. Lyon, C. H. Ma, D. A. Rasmussen, C. R. Schaich, J. B. Wilgen and J. L. Yarber, *Long Pulse Discharges Sustained by Second Harmonic Electron Cyclotron Heating Using a 35GH$_Z$ Gyrotron in the Advanced Toroidal Facility*; Sep. 1992

NIFS-184 S. Okamura, K. Hanatani, K. Nishimura, R. Akiyama, T. Amano, H. Arimoto, M. Fujiwara, M. Hosokawa, K. Ida, H. Idei, H. Iguchi, O. Kaneko, T. Kawamoto, S. Kubo, R. Kumazawa, K. Matsuoka, S. Morita, O. Motojima, T. Mutoh, N. Nakajima, N. Noda, M. Okamoto, T. Ozaki, A. Sagara, S. Sakakibara, H. Sanuki, T. Seki, T. Shoji, F. Shimbo, C. Takahashi, Y. Takeiri, Y. Takita, K. Toi, K. Tsumori, M. Ueda, T. Watari, H. Yamada and I. Yamada, *Heating Experiments Using Neutral Beams with Variable Injection Angle and ICRF Waves in CHS* ; Sep. 1992

NIFS-185 H. Yamada, S. Morita, K. Ida, S. Okamura, H. Iguchi, S. Sakakibara, K. Nishimura, R. Akiyama, H. Arimoto, M. Fujiwara, K. Hanatani, S. P. Hirshman, K. Ichiguchi, H. Idei, O. Kaneko, T. Kawamoto, S. Kubo, D. K. Lee, K. Matsuoka, O, Motojima, T. Ozaki, V. D. Pustovitov, A. Sagara, H. Sanuki, T. Shoji, C. Takahashi, Y. Takeiri, Y. Takita, S. Tanahashi, J. Todoroki, K. Toi, K. Tsumori, M. Ueda and I. Yamada, *MHD and Confinement Characteristics in the High-β Regime on the CHS Low-Aspect-Ratio Heliotron / Torsatron* ; Sep. 1992

NIFS-186 S. Morita, H. Yamada, H. Iguchi, K. Adati, R. Akiyama, H. Arimoto, M. Fujiwara, Y. Hamada, K. Ida, H. Idei, O. Kaneko, K. Kawahata,

T. Kawamoto, S. Kubo, R. Kumazawa, K. Matsuoka, T. Morisaki, K. Nishimura, S. Okamura, T. Ozaki, T. Seki, M. Sakurai, S, Sakakibara, A. Sagara, C. Takahashi, Y. Takeiri, H. Takenaga, Y. Takita, K. Toi, K. Tsumori, K. Uchino, M. Ueda, T. Watari, I. Yamada, *A Role of Neutral Hydrogen in CHS Plasmas with Reheat and Collapse and Comparison with JIPP T-IIU Tokamak Plasmas* ; Sep. 1992

NIFS-187 K. Ioth, S.-I. Itoh, A. Fukuyama, M. Yagi and M. Azumi, *Model of the L-Mode Confinement in Tokamaks* ; Sep. 1992

NIFS-188 K. Itoh, A. Fukuyama and S.-I. Itoh, *Beta-Limiting Phenomena in High-Aspect-Ratio Toroidal Helical Plasmas*; Oct. 1992

NIFS-189 K. Itoh, S. -I. Itoh and A. Fukuyama, *Cross Field Ion Motion at Sawtooth Crash* ; Oct. 1992

NIFS-190 N. Noda, Y. Kubota, A. Sagara, N. Ohyabu, K. Akaishi, H. Ji, O. Motojima, M. Hashiba, I. Fujita, T. Hino, T. Yamashina, T. Matsuda, T. Sogabe, T. Matsumoto, K. Kuroda, S. Yamazaki, H. Ise, J. Adachi and T. Suzuki, *Design Study on Divertor Plates of Large Helical Device (LHD)* ; Oct. 1992

NIFS-191 Y. Kondoh, Y. Hosaka and K. Ishii, *Kernel Optimum Nearly-Analytical Discretization (KOND) Algorithm Applied to Parabolic and Hyperbolic Equations* : Oct. 1992

NIFS-192 K. Itoh, M. Yagi, S.-I. Itoh, A. Fukuyama and M. Azumi, *L-Mode Confinement Model Based on Transport-MHD Theory in Tokamaks* ; Oct. 1992

NIFS-193 T. Watari, *Review of Japanese Results on Heating and Current Drive* ; Oct. 1992

NIFS-194 Y. Kondoh, *Eigenfunction for Dissipative Dynamics Operator and Attractor of Dissipative Structure* ; Oct. 1992

NIFS-195 T. Watanabe, H. Oya, K. Watanabe and T. Sato, *Comprehensive Simulation Study on Local and Global Development of Auroral Arcs and Field-Aligned Potentials* ; Oct. 1992

NIFS-196 T. Mori, K. Akaishi, Y. Kubota, O. Motojima, M. Mushiaki, Y. Funato and Y. Hanaoka, *Pumping Experiment of Water on B and LaB_6 Films with Electron Beam Evaporator* ; Oct., 1992

NIFS-197 T. Kato and K. Masai, *X-ray Spectra from Hinotori Satellite and Suprathermal Electrons* ; Oct. 1992

NIFS-198 K. Toi, S. Okamura, H. Iguchi, H. Yamada, S. Morita, S. Sakakibara, K. Ida, K. Nishimura, K. Matsuoka, R. Akiyama, H. Arimoto, M. Fujiwara, M. Hosokawa, H. Idei, O. Kaneko, S. Kubo, A. Sagara, C. Takahashi, Y. Takeiri, Y. Takita, K. Tsumori, I. Yamada and H. Zushi, *Formation of H-mode Like Transport Barrier in the CHS Heliotron / Torsatron* ; Oct. 1992

NIFS-199 M. Tanaka, *A Kinetic Simulation of Low-Frequency Electromagnetic Phenomena in Inhomogeneous Plasmas of Three-Dimensions* ; Nov. 1992

NIFS-200 K. Itoh, S.-I. Itoh, H. Sanuki and A. Fukuyama, *Roles of Electric Field on Toroidal Magnetic Confinement*, Nov. 1992

NIFS-201 G. Gnudi and T. Hatori, *Hamiltonian for the Toroidal Helical Magnetic Field Lines in the Vacuum*; Nov. 1992

NIFS-202 K. Itoh, S.-I. Itoh and A. Fukuyama, *Physics of Transport Phenomena in Magnetic Confinement Plasmas*; Dec. 1992

NIFS-203 Y. Hamada, Y. Kawasumi, H. Iguchi, A. Fujisawa, Y. Abe and M. Takahashi, *Mesh Effect in a Parallel Plate Analyzer*; Dec. 1992

NIFS-204 T. Okada and H. Tazawa, *Two-Stream Instability for a Light Ion Beam -Plasma System with External Magnetic Field;* Dec. 1992

NIFS-205 M. Osakabe, S. Itoh, Y. Gotoh, M. Sasao and J. Fujita, *A Compact Neutron Counter Telescope with Thick Radiator (Cotetra) for Fusion Experiment*; Jan. 1993

NIFS-206 T. Yabe and F. Xiao, *Tracking Sharp Interface of Two Fluids by the CIP (Cubic-Interpolated Propagation) Scheme*, Jan. 1993

NIFS-207 A. Kageyama, K. Watanabe and T. Sato, *Simulation Study of MHD Dynamo : Convection in a Rotating Spherical Shell*; Feb. 1993

NIFS-208 M. Okamoto and S. Murakami, *Plasma Heating in Toroidal Systems*; Feb. 1993

NIFS-209 K. Masai, *Density Dependence of Line Intensities and Application to Plasma Diagnostics*; Feb. 1993

NIFS-210 K. Ohkubo, M. Hosokawa, S. Kubo, M. Sato, Y. Takita and T. Kuroda, *R&D of Transmission Lines for ECH System* ; Feb. 1993

NIFS-211 A. A. Shishkin, K. Y. Watanabe, K. Yamazaki, O. Motojima, D. L. Grekov, M. S. Smirnova and A. V. Zolotukhin, *Some Features of Particle Orbit Behavior in LHD Configurations*; Mar. 1993

NIFS-212 Y. Kondoh, Y. Hosaka and J.-L. Liang, *Demonstration for Novel Self-organization Theory by Three-Dimensional Magnetohydrodynamic Simulation*; Mar. 1993

NIFS-213 K. Itoh, H. Sanuki and S.-I. Itoh, *Thermal and Electric Oscillation Driven by Orbit Loss in Helical Systems*; Mar. 1993

NIFS-214 T. Yamagishi, *Effect of Continuous Eigenvalue Spectrum on Plasma Transport in Toroidal Systems*; Mar. 1993

NIFS-215 K. Ida, K. Itoh, S.-I.Itoh, Y. Miura, JFT-2M Group and A. Fukuyama, *Thickness of the Layer of Strong Radial Electric Field in JFT-2M H-mode Plasmas*; Apr. 1993

NIFS-216 M. Yagi, K. Itoh, S.-I. Itoh, A. Fukuyama and M. Azumi, *Analysis of Current Diffusive Ballooning Mode*; Apr. 1993

NIFS-217 J. Guasp, K. Yamazaki and O. Motojima, *Particle Orbit Analysis for LHD Helical Axis Configurations* ; Apr. 1993

NIFS-218 T. Yabe, T. Ito and M. Okazaki, *Holography Machine HORN-1 for Computer-aided Retrieve of Virtual Three-dimensional Image* ; Apr. 1993

NIFS-219 K. Itoh, S.-I. Itoh, A. Fukuyama, M. Yagi and M. Azumi, *Self-sustained Turbulence and L-Mode Confinement in Toroidal Plasmas* ; Apr. 1993

NIFS-220 T. Watari, R. Kumazawa, T. Mutoh, T. Seki, K. Nishimura and F. Shimpo, *Applications of Non-resonant RF Forces to Improvement of Tokamak Reactor Performances Part I: Application of Ponderomotive Force* ; May 1993

NIFS-221 S.-I. Itoh, K. Itoh, and A. Fukuyama, *ELMy-H mode as Limit Cycle and Transient Responses of H-modes in Tokamaks* ; May 1993

NIFS-222 H. Hojo, M. Inutake, M. Ichimura, R. Katsumata and T. Watanabe, *Interchange Stability Criteria for Anisotropic Central-Cell Plasmas in the Tandem Mirror GAMMA 10 ;* May 1993

NIFS-223 K. Itoh, S.-I. Itoh, M. Yagi, A. Fukuyama and M. Azumi, *Theory of Pseudo-Classical Confinement and Transmutation to L-Mode;* May 1993